J. Fluid Mech. (1990), *vol.* 219, *pp.* 143–179
Printed in Great Britain

Bubble entrainment by the impact of drops on liquid surfaces

By HASAN N. OĞUZ AND ANDREA PROSPERETTI
Department of Mechanical Engineering, The Johns Hopkins University, Baltimore, MD 21218, USA

(Received 19 May 1989 and in revised form 2 March 1990)

The impact of a drop on the plane surface of the same liquid is studied numerically. The accuracy of the calculation is substantiated by its good agreement with available experimental data. An attempt is made to explain the recent observation that, in a restricted range of drop radii and impact velocities, small air bubbles remain entrained in the liquid. The implications of this process for the underwater sound due to rain are considered. The numerical approach consists of a new formulation of the boundary-element method which is explained in detail. Techniques to stabilize the calculation in the presence of strong surface-tension effects are also described.

1. Introduction

The fact that a water drop impinging on a water surface may lead to the entrapment of an air bubble at the bottom of the crater that it produces has been known for some time (Franz 1959). However, the intricate features of this phenomenon have only recently been clarified by Pumphrey & Crum (1988; see also Pumphrey, Crum & Bjørnø 1989) in the course of an experimental study of the mechanism of rain noise. While their results will be summarized in some detail in the next section, we mention here that they discovered that, far from being a random event as suggested by Franz, bubbles remain entrapped under very well-defined conditions and lead to a very substantial noise emission in the water. The significant consequences of this finding for the generation of underwater noise by rain have been addressed elsewhere (Prosperetti, Pumphrey & Crum 1989) and are summarized in the last section of this paper. Here we wish to study theoretically the fluid dynamics of crater formation and bubble entrapment and develop a qualitative understanding of the physics involved in these processes. Our main tool is numerical, and the dominant effect of surface tension on the process has required the development of a stable boundary-integral method which is of interest in itself and is described in detail.

The study of drop impact on liquid surfaces has a long history that goes back to the end of the last century when Worthington (1894) studied the process by means of single-flash photography. Quite famous are also the high-speed photographs of Edgerton (Edgerton & Killian 1939). These researchers, as well as others such as Engel (1967) and Macklin & Metaxas (1976), studied, however, impacts at relatively high speeds and therefore missed many interesting aspects of the process that were recently identified by Pumphrey and Crum. One of the early applications of the MAC code also dealt with drop impact on a liquid layer (Harlow & Shannon 1967*a*, *b*), but again, as pointed out by Carroll & Mesler (1981*a*, *b*), many subtleties were missed because of the incomplete treatment of surface-tension phenomena. The same

problems have been encountered quite recently by Nystuen (1986), Nystuen & Farmer (1988), and Hashimoto & Sudo (1980) with their updated versions of the MAC code. The last authors were able, however, to describe the entrapment of secondary bubbles upon the collapse of the liquid column that forms with the filling of the crater (see §2).

As alrcady observed, the main difficulty to overcome in the numerical simulation of the process is the treatment of surface-tension effects. In an earlier study (Oğuz & Prosperetti 1989) we have shown that, in most practical circumstances, surface tension causes liquid–liquid contact to occur not only at the point of first contact between the drop and the receiving liquid, but over an extended area. In that paper the intricacies of this phenomenon were explored in detail. Here we shall bypass those aspects by adopting an initial condition in which the drop contacts the plane liquid surface over a sufficiently large area. Even with this approximation, surface tension causes serious difficulties. In a model such as the present one in which capillarity is accounted for but not viscosity, an attempt to obtain a high surface resolution leads to the appearance of short capillary waves which have a very large frequency. As a consequence, the ratio between the shortest and longest timescales is very small and the problem is numerically stiff. Time steps of a reasonable magnitude can only be used in the integration by introducing a suitable smoothing action on these very short waves. We believe that the procedures that we have developed for this purpose, described in §6, can be applied to a variety of other problems in which surface tension plays a major role.

2. Summary of the experimental results

In order to set the developments of this paper against a suitable background it is useful to give here a summary of the experimental findings of Pumphrey & Crum (1988; see also Pumphrey *et al.* 1989; Prosperetti *et al.* 1989). One of their most unexpected results is the fact that bubbles are entrapped in the crater produced by the impacting drops only in a sharply delimited region of parameter space, which we shall refer to as the *bubble region*. If, at the moment of impact, the drop is assumed to be spherical, then two parameters are sufficient to completely characterize an impact event. They can be conveniently chosen to be the impact velocity U and the drop radius R or, alternatively, the Froude number Fr

$$Fr = \frac{U^2}{2gR}, \tag{2.1}$$

and the Weber number We

$$We = \frac{2\rho U^2 R}{\sigma}. \tag{2.2}$$

In the (R, U)-plane shown in figure 1 the dashed line shows the terminal velocity of rain drops. To the right of this line a regular process of bubble entrainment takes place only in the shaded region. This figure shows the original data of Pumphrey and Crum and two continuous lines obtained by a best fit to the data. Below the shaded area the crater is too shallow to give rise to a bubble, while above it its energy is too large. Two typical high-speed sequences of drop impacts with and without bubble formation are shown in figures 2(*a*) and 3(*a*) taken from Pumphrey & Crum (1988). In the first case the cavity takes on a more or less cylindrical shape with a rounded nose. The liquid motion stops and reverses at different times at different positions. While the tip of the cavity keeps growing, the sidewalls reverse their outward motion

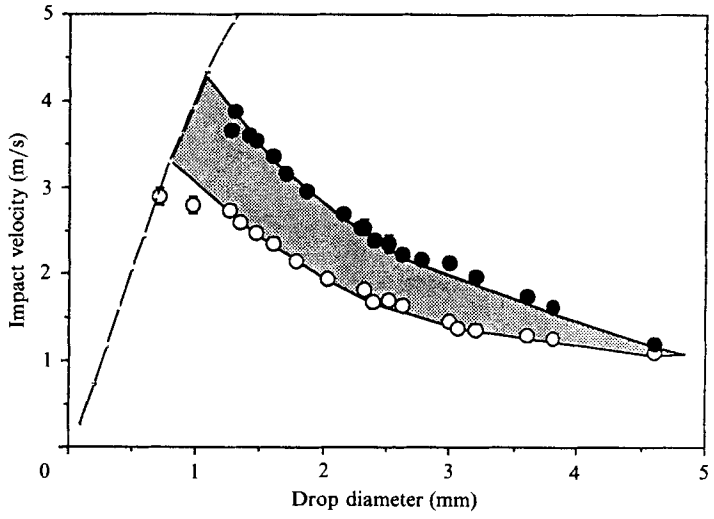

FIGURE 1. In the space of the parameters R (drop radius) and U (drop impact velocity) an air bubble is entrained only in the shaded region. Here the symbols are the data of Pumphrey and Crum (Prosperetti *et al.* 1989). The lines are best fits to the data obtained by neglecting the two leftmost data points that appear to be affected by a large error.

and start moving in with a velocity that increases with depth. The consequence of this situation is the curious funnel shape appearing in the last few frames, which leads to a bubble through the pinching-off of the narrow tip.

The cavity dynamics in the higher impact velocity case of figure 3(*a*) is quite different. The cavity is very nearly hemispherical with a pronounced splash around its rim and the liquid, aside from some capillary waves, seems to reverse its motion more or less simultaneously everywhere around the crater's surface. This leads to a filling of the cavity which starts at the bottom, where the potential energy is highest, and causes an upward-directed jet. One way in which the difference between figures 2(*a*) and 3(*a*) can be described is by saying that, while the impacting drop is a source of both mass and momentum for the receiving liquid, the mass-source aspect dominates at high velocity, while the momentum-source aspect, with its downward direction, is the most important feature at moderate impact velocities. Movies in which the impacting drop is coloured show that, in the high-velocity case, the drop material spreads rather evenly over the surface of the cavity.† The indirect evidence that we have seems to indicate instead that, at the moderate impact velocities that give rise to bubbles, the drop material remains collected at the bottom of the cavity.

The vertical lines to the right of the physical event in the photographs of figures 2(*a*) and 3(*a*) reproduce the screen of an oscilloscope driven by a hydrophone visible in the right-hand corner of the frames of figure 2(*a*). It is clear that the detachment of the bubble in figure 2(*a*) is accompanied by a substantial acoustic emission, while all other phases of the process, including the impact itself, are relatively silent.

Figure 4 is a replotting of figure 1 in terms of Fr and We. The continuous lines are given by power-law relations of the form

$$We = A\,Fr^{\alpha}. \tag{2.3}$$

† We are indebted to Dr G. Chahine for making available to us his films.

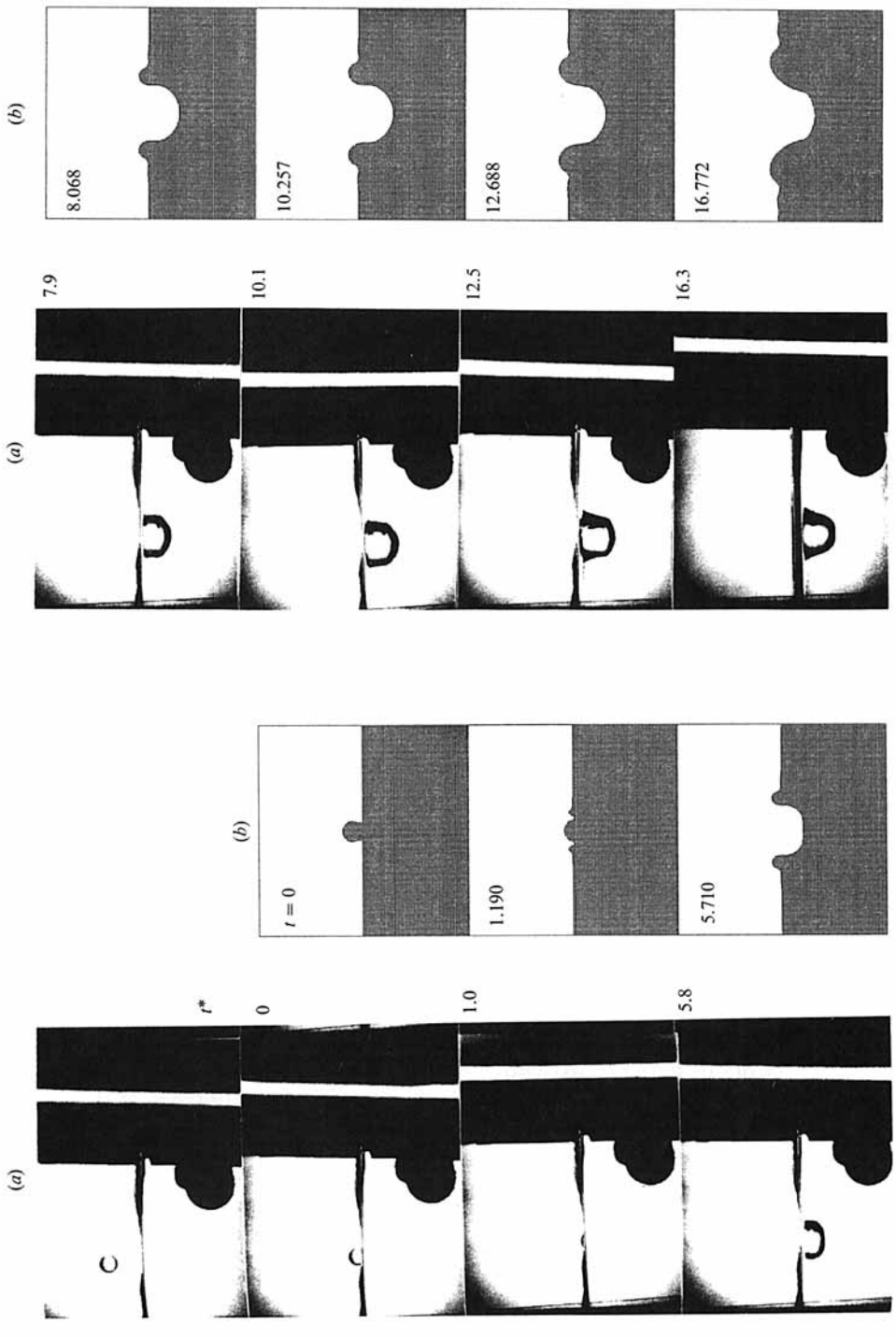
(a)
t*
0
1.0
5.8
(b)
t = 0
1.190
5.710
(a)
7.9
10.1
12.5
16.3
(b)
8.068
10.257
12.688
16.772

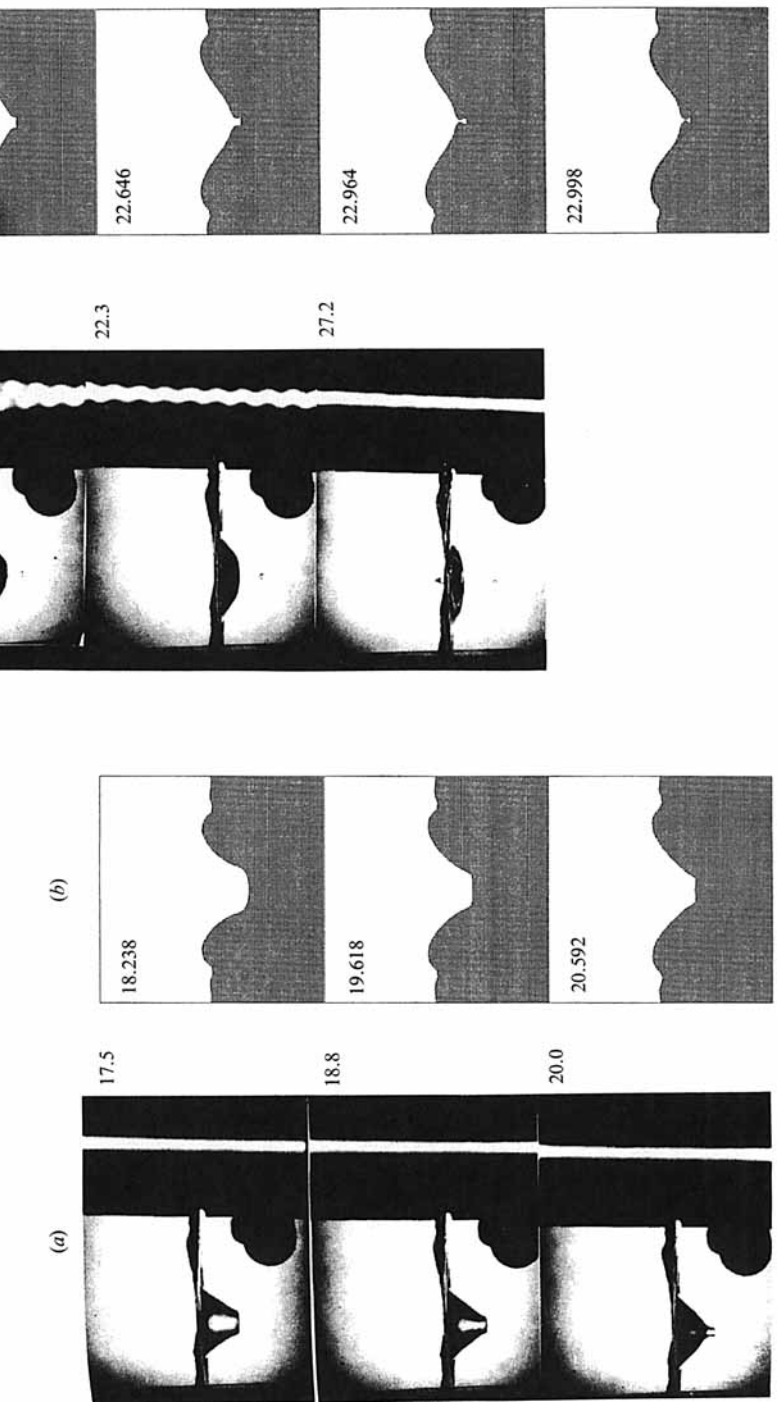

FIGURE 2. Comparison between (*a*) the high-speed film of Pumphrey & Crum (1988) and (*b*) the computed results of the present study for the impact of a drop with a radius $R = 1.9$ mm and impact velocity $U = 1.53$ m/s. The times indicated are in the dimensionless units $t_* = Ut/R$, with the time origin at the instant of impact. This sequence is typical of impact events in which a bubble is entrained. The width of the frames showing the computed results is 20 dimensionless units.

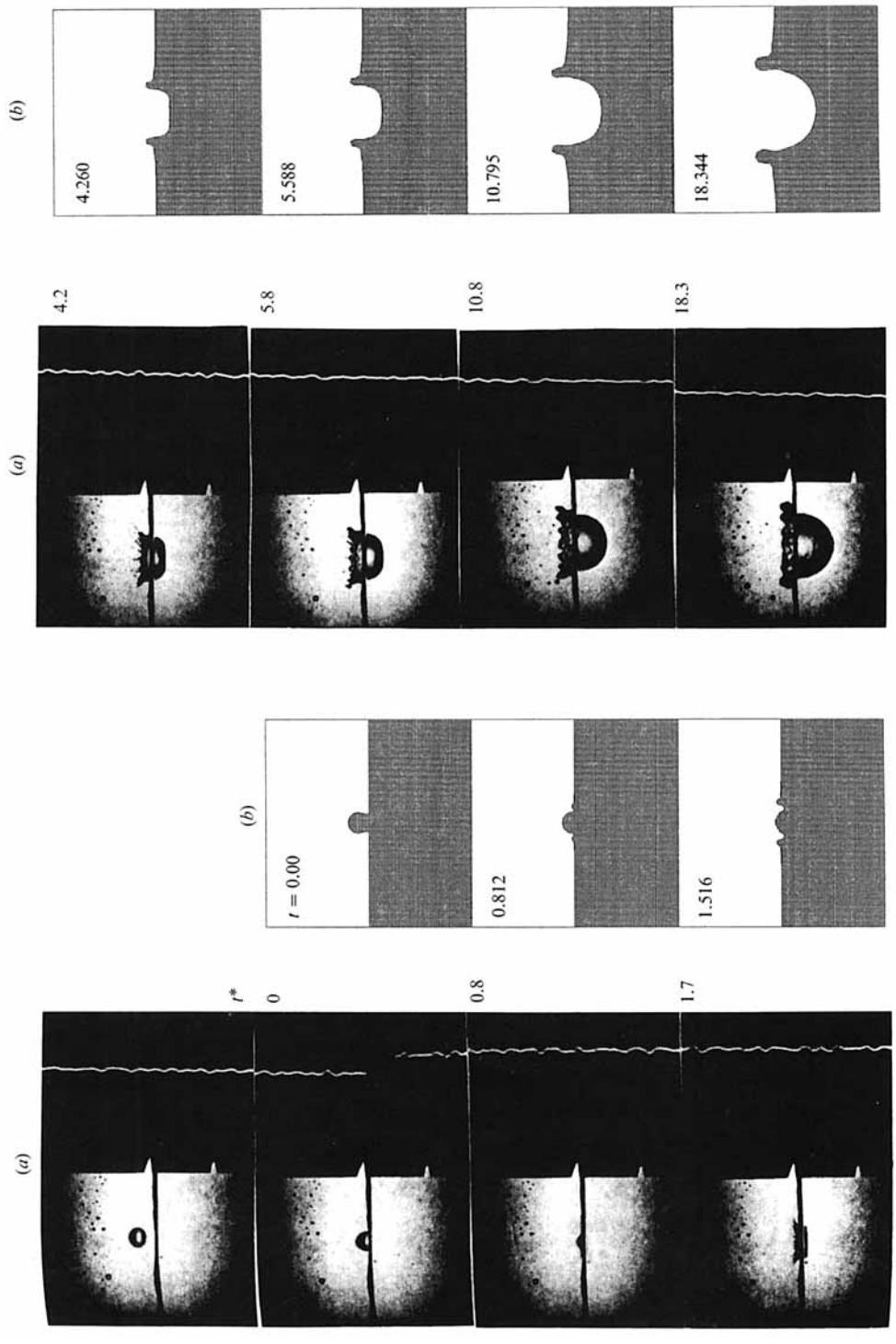
(a)
t*
0
0.8
1.7
(b)
t = 0.00
0.812
1.516
(a)
4.2
5.8
10.8
18.3
(b)
4.260
5.588
10.795
18.344

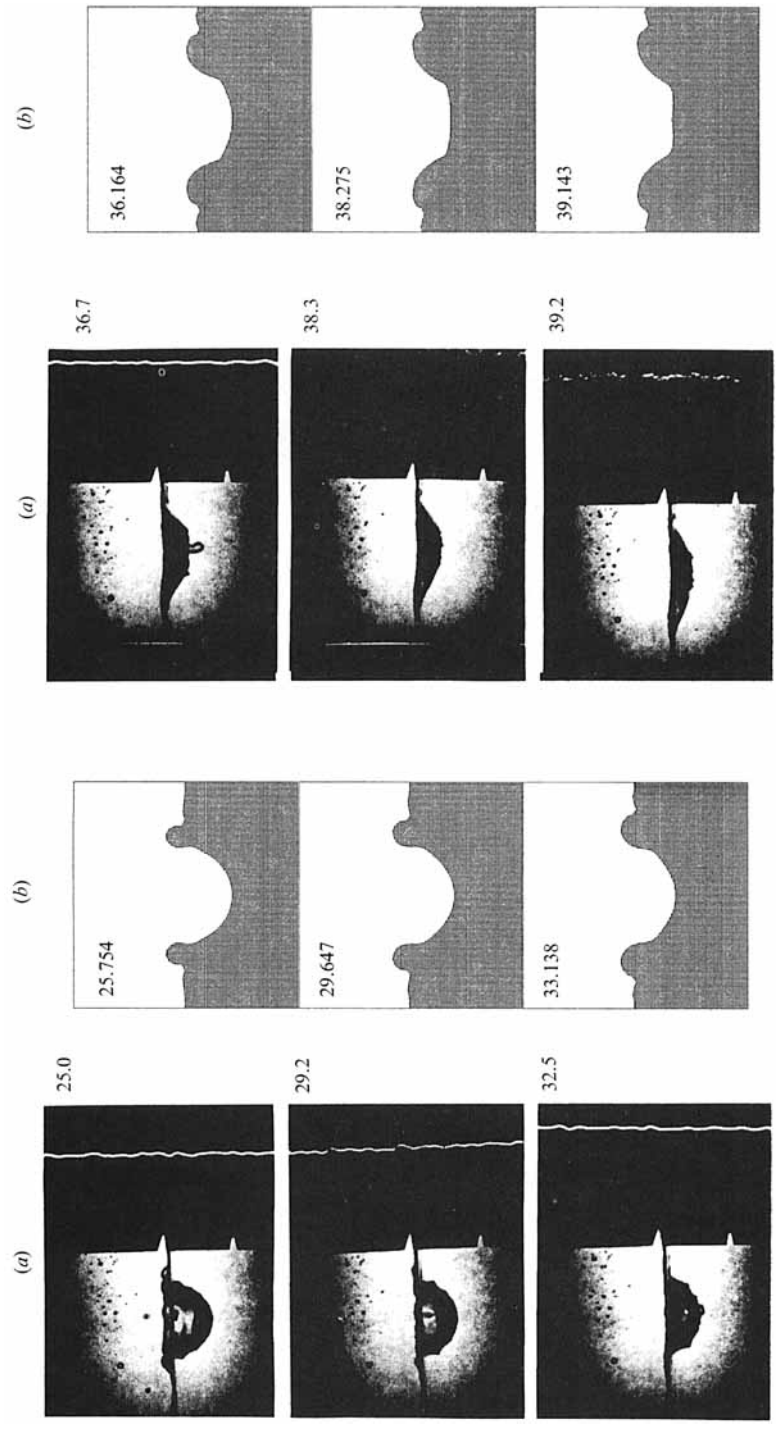

FIGURE 3. For caption see next page.

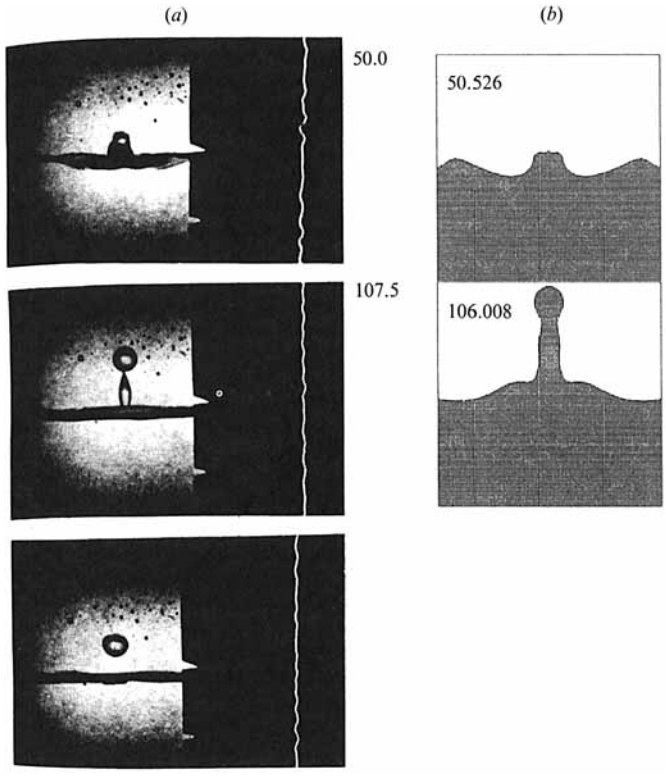

FIGURE 3. Comparison between (*a*) the high-speed film of Pumphrey & Crum (1988) and (*b*) the computed results of the present study for the impact of a drop with a radius $R = 2.9$ mm and impact velocity $U = 2.40$ m/s. The times indicated are in the dimensionless units $t_* = Ut/R$, with the time origin at the instant of impact. This sequence is typical of impact events in which the impact velocity is too large for a bubble to be entrained. The width of the frames showing the computed results is 20 dimensionless units.

If the two data points at the smallest values of the radii, which are difficult to obtain experimentally and appear in figure 1 to be affected by a relatively large error, are discarded, a least-square fit gives $A = 48.3$ and $\alpha = 0.247$, and $A = 41.3$ and $\alpha = 0.179$ for the upper and lower lines, respectively.

3. Qualitative mechanism of bubble entrapment

Before embarking in a complex numerical study of the process at hand, it is useful to try to understand its main features in qualitative physical terms.

Let us first consider the possible origin of the upper boundary in figures 1 or 4, which constitutes an upper bound for bubble entrapment. On the basis of the discussion of the previous section it seems reasonable to postulate that, if the drop material spreads essentially over the entire surface of the crater, the crater will grow radially and no bubble will be entrapped. For a given radius, the upper limit to the impact velocity arising from this argument is therefore

$$R_{\rm sp} \sim R_{\rm c}, \tag{3.1}$$

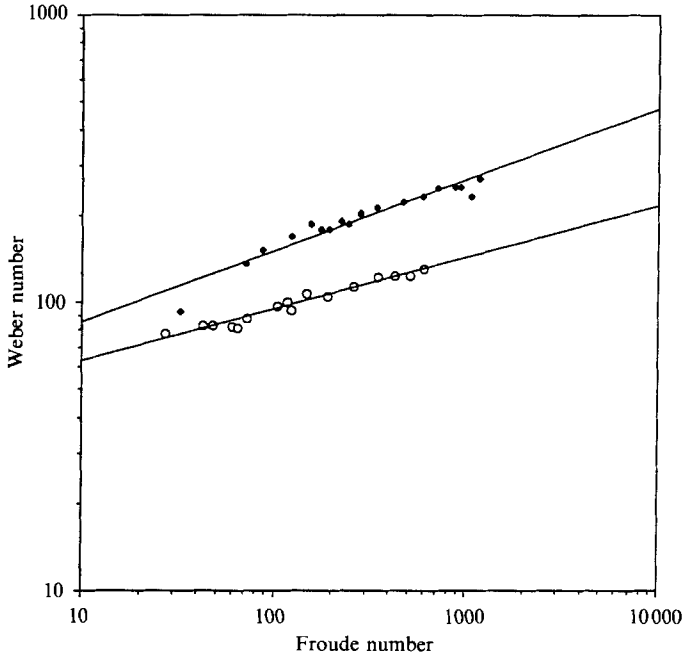

FIGURE 4. The two boundaries of the bubble region shown in figure 1 are plotted in terms of the Froude number $U^2/2gR$ and Weber number $2\rho U^2 R/\sigma$.

where R_{sp} is a characteristic linear dimension of the region over which the drop material spreads and R_c is the radius of the crater. This equation should correspond to the upper boundary in figures 1 or 4.

In order to estimate the crater radius we equate the energy of the drop just before the impact, $\frac{1}{2}(\frac{4}{3}\pi R^3)\,U^2$, to the potential energy stored in the crater at the moment in which the motion reverses itself. With the neglect of surface energy, which can be shown to represent only a small fraction of the total energy in the crater, and the assumption of a hemispherical shape, it is easy to find that

$$R_c \sim RFr^{\frac{1}{4}}. \tag{3.2}$$

A more realistic assumption about the shape of the crater would only introduce numerical factors of order one. As a matter of fact, it turns out that this simple relation fits extremely well all the data collected by Pumphrey & Crum (1988).

To estimate the spreading radius we may proceed as follows. During the impact, the retarding force acting on the drop can be estimated to be of the order of the virtual mass, $\frac{2}{3}\pi\rho R^3$, times the acceleration $(U/R)\,U$. This estimate assumes that the motion with velocity U is brought to rest in a time of the order of R/U. The force that restrains the spreading of the droplet material is surface tension, so that we are led to the balance

$$\frac{U}{R}(\rho R^3 U) \sim \nabla(\sigma r^2)|_{r=R_{sp}}. \tag{3.3}$$

In writing this force balance we assume that the drop material has spread over the walls of the crater so that the restraining effect of surface tension acts predominantly

in the vertical direction as the virtual mass acceleration in the left-hand side. From this relation it follows immediately that

$$R_{\rm sp} \sim R\,We. \tag{3.4}$$

Another way in which this relation can be justified is the following. The contact line between the drop material and the receiving fluid has a perimeter of order $R_{\rm sp}$, so that the surface-tension force acting on it is of the order of $\sigma R_{\rm sp}$. On the other hand, the total pressure acting on the inside of the drop surface is of the order of the stagnation pressure ρU^2 times the drop area R^2. Again, the balance of these two forces leads to (3.4).

Substituting now (3.2) and (3.4) into (3.3) we are led to the following relation for the upper boundary of the bubble-entraining region:

$$We \sim Fr^{\frac{1}{4}}. \tag{3.5}$$

Experimentally, the exponent giving the best fit to the data of figure 4 has the value 0.247, which is quite compatible with the value 0.25 given by this relation.

In order to formulate a similar argument for the lower boundary of the bubble region in figures 1 or 4 we have found it necessary to appeal to the experimental observation (H. C. Pumphrey, private communication) that the time $t_{\rm M}$ to maximum growth of the crater scales proportionally to $RU^{\frac{1}{3}}$. Putting this relation in dimensionless form one finds the unique answer

$$\frac{Ut_{\rm M}}{R} \sim \left(\frac{U}{c_{\rm m}}\right)^{\frac{4}{3}}, \tag{3.6}$$

where $c_{\rm m} = (4g\sigma/\rho)^{\frac{1}{4}}$ is the minimum phase velocity of capillary–gravity surface waves. We have been unable to derive this relation on the basis of a simple physical argument. However, we have the impression that its success in correlating the data is more related to a numerical coincidence in a restricted range of the variables than to a fundamental physical law. Be that as it may, it is not unreasonable to find a dependence of $t_{\rm M}$ upon $c_{\rm m}$ since the energy stored in the crater can only be carried away by surface waves, a process that must be limited by the slowest velocity of propagation for these waves.

With the previous relation we can formulate the following argument. At the same time as the crater grows, a capillary wave is established on its bottom by the impact. The initial phase of this wave is such that the water motion is downward. If this downward motion reverses before the crater has grown to its maximum depth, the precise timing necessary for the entrainment of a bubble will be disrupted and the crater will fill from the bottom with an upward-directed wave crest instead. The condition for bubble entrapment based on this argument is therefore

$$t_{\rm w} > t_{\rm M},$$

where $t_{\rm w}$ is the period of the capillary wave at the bottom of the crater which can be estimated by $[(\sigma/\rho)\,k^3]^{-\frac{1}{2}}$, with the wavenumber $k \sim 1/R_{\rm sp}$. In this way, the marginal condition for bubble entrapment is found to be

$$We \sim Fr^{\frac{1}{5}}. \tag{3.7}$$

The exponent of 0.2 is quite comparable with the value 0.179 obtained from a best fit to the data.

4. Mathematical formulation

We take the drop and the receiving liquid to be of the same fluid which, for the applications we have in mind, will be water. The impact velocities we consider are of the order of a few metres per second and the drop radii of a few millimetres so that a Reynolds number defined by RU/ν has a value of the order of 10^3 or higher. Since, furthermore, the process is highly transient, viscous effects can be neglected. The effects of compressibility are important on timescales of the order of the acoustic travel time in the drop, which can be measured in microseconds. Since we are concerned with the evolution of the system over much longer times, these effects can be neglected and the liquid taken to be incompressible.

In an earlier paper (Oğuz & Prosperetti 1989) we have studied in considerable detail the early stages of the impact and we have found a very complex behaviour. Briefly, a number of very small air bubbles are entrained under the drop, and liquid–liquid contact occurs at a number of places in addition to the point of first contact. The situation can be simulated by a weak vortex sheet that forms between the two liquid masses brought into contact. Some preliminary results show that the strength of this vortex sheet is very small for the range of impact velocities that we consider here. Accordingly, we shall take the motion to be irrotational everywhere and the velocity potential ϕ to satisfy Laplace's equation,

$$\nabla^2\phi = 0. \tag{4.1}$$

We consider the drop to be spherical at the moment of impact with the plane liquid surface. This assumption is borne out by the photographic results for small droplets. Larger drops do exhibit some shape oscillations, as can be seen in the first frame of figure 3(*a*), but they cannot be of any great importance since the numerical results that we find reproduce to such a good approximation the experimental ones.

To avoid the simulation of the early stages of the process that, as was mentioned, are extremely complicated, we start the calculation from a configuration in which the drop has a non-vanishing area of contact with the receiving liquid.

The plane surface is taken to be the (x, y)-plane $z = 0$ and the z-axis is directed upward against gravity. We use the impact velocity U as a reference velocity and the drop radius R as the reference length. Time is therefore rendered dimensionless with respect to the fundamental timescale R/U. The initial condition is that the drop material is in solid-body motion with unit dimensionless velocity, while the receiving liquid is at rest, i.e.

$$\phi = -z, \quad 0 \leqslant z \leqslant 2, \qquad \phi = 0, \quad z \leqslant 0. \tag{4.2}$$

Again this is an approximation because the compressional wave that sweeps through the receiving liquid at the moment of impact will set a non-zero value of the velocity potential, but again this effect does not seem to be of any great importance in view of the very good agreement between computations and experiment.

By use of the Bernoulli integral to express the pressure on the liquid side of the interface, the rate of change of the potential carried by a Lagrangian surface particle is found to be given by

$$\left.\frac{\mathrm{d}\phi}{\mathrm{d}t}\right|_S = \tfrac{1}{2}|\nabla\phi|^2 + \frac{1}{2Fr}z + \frac{2}{We}\mathscr{C}, \tag{4.3}$$

where the Froude and Weber numbers Fr and We have been defined in (2.1) and (2.2), $\mathscr{C}$ denotes the local curvature, positive when the centres of curvature are in the

liquid, and the subscript S denotes the generic surface particle. The position of the Lagrangian surface particles is obtained by integrating

$$\frac{\mathrm{d}\boldsymbol{x}|_S}{\mathrm{d}t} = \boldsymbol{\nabla}\phi|_S. \tag{4.4}$$

This relation is not equivalent to the kinematic boundary condition because it also contains a specific choice for the tangential velocity of the interface, but this fact is clearly of no consequence.

5. A novel boundary-integral method

Since our aim is to determine the successive configurations of the interface, we only need to be concerned with the values of the velocity field on the free surface. This circumstance renders the use of a boundary-integral formulation very attractive.

Over the past ten years the boundary-integral formulation has received considerable attention and has been successfully used in several problems such as breaking plungers (Dommermuth *et al.* 1988). The particular method we choose is similar to the one developed by Baker, Meiron & Orszag (1980) for two-dimensional flows, although it differs from that one in important details as will be shown. Furthermore, the present application is particularly demanding in view of the critical effect of surface tension on our process. As noted above, and as documented in the literature (Pullin 1982; Lundgren & Mansour 1988), severe stability problems arise on attempting to include surface-tension effects in an inviscid formulation. We have succeeded in developing stable and relatively robust methods to handle this problem. This constitutes one of the novel aspects of our technique.

Since ϕ satisfies the Laplace equation, so do its Cartesian derivatives

$$\nabla^2 \frac{\partial \phi}{\partial x_i} = 0.$$

In the (x, y)-plane Cartesian coordinates are related to cylindrical coordinates by the relations

$$\frac{\partial \phi}{\partial x_1} = \cos\psi \frac{\partial \phi}{\partial r}, \quad \frac{\partial \phi}{\partial x_2} = \frac{\partial \phi}{\partial z},$$

where ψ is the azimuthal angle and r and z are cylindrical coordinates. By a straightforward application of the form of Green's identity appropriate to the present axisymmetric problem (see the Appendix and e.g. Jaswon & Symm 1977) to the velocity components $\partial\phi/\partial x_i$ and some manipulations we then obtain

$$\frac{\partial \phi}{\partial z} = -\int_S \left(\frac{\partial v_r}{\partial s} + \frac{1}{r}\frac{\partial r}{\partial s} v_r\right) G \,\mathrm{d}s - \int_S v_z H \,\mathrm{d}s, \tag{5.1a}$$

$$\frac{\partial \phi}{\partial r} = \int_S \left(\frac{\partial v_z}{\partial s} + \frac{1}{r}\frac{\partial z}{\partial s} v_r\right) F \,\mathrm{d}s - \int_S v_r E \,\mathrm{d}s, \tag{5.1b}$$

where G, H, E and F are known functions involving elliptic integrals of first, second and third kind, explicit forms for which are given in the Appendix.

Next, we introduce a vortex-sheet strength Γ defined by

$$\Gamma = \frac{\partial}{\partial s}(\phi - \phi^-), \tag{5.2}$$

where ϕ is the potential in the fluid region of interest and ϕ^- represents the potential associated with a fluid on the other side of the interface. While in the present case this fluid is fictitious in that it only provides a constant pressure and has no dynamical effects, the technique that we describe can also be adapted to a two-fluid problem as will be seen. We now define a mean velocity by summing the surface velocities on the two sides of the interface to find

$$\phi_z^{\mathrm{m}} \equiv \frac{\partial \phi}{\partial z} + \frac{\partial \phi^-}{\partial z} = -\int_S \frac{1}{r}\frac{\partial}{\partial s}(r t_r \Gamma)\, G\, \mathrm{d}s - \int_S t_z \Gamma H\, \mathrm{d}s, \tag{5.3a}$$

$$\phi_r^{\mathrm{m}} \equiv \frac{\partial \phi}{\partial r} + \frac{\partial \phi^-}{\partial r} = \int_S \frac{1}{r}\frac{\partial}{\partial s}(r t_z \Gamma)\, F\, \mathrm{d}s - \int_S t_r \Gamma E\, \mathrm{d}s, \tag{5.3b}$$

and we note that Γ is related to ϕ by

$$\Gamma = 2\frac{\partial \phi}{\partial s} - (t_z \phi_z^{\mathrm{m}} + t_r \phi_r^{\mathrm{m}}), \tag{5.4}$$

where t_r, t_z are the component of a unit vector tangent to the interface in a meridian plane. How the value of ϕ is calculated depends on whether one is dealing with a real or fictitious second fluid. In the present problem we use (4.3), so that the correct dynamical boundary condition is imposed. Use of a different equation to update the surface value of ϕ renders this method suitable for a two-fluid problem as well.

Conceptually, substitution of (5.3*a*, *b*) into (5.4) leads to a Fredholm equation of the second kind for Γ. This is interesting and avoids the potential difficulties that might arise from the first-kind equations that would result from a simpler approach such as that of Oğuz & Prosperetti (1989). For practical purposes, however, rather than dealing with this integral equation directly, it is more convenient to solve (5.3*a*, *b*) and (5.4) iteratively.

This method is very similar to the vortex velocity method described in Baker, Meiron & Orszag (1984). Its main advantage over that method is that, after convergence, the convective surface velocities are readily available from

$$v_z = \tfrac{1}{2}(\phi_z^{\mathrm{m}} - \Gamma t_r), \quad v_r = \tfrac{1}{2}(\phi_r^{\mathrm{m}} - \Gamma t_z). \tag{5.5}$$

In the approach of Baker *et al.*, on the other hand, these velocity components must be obtained by first calculating the vector potential, which requires the evaluation of an integral for each field point, and then carrying out a numerical differentiation with an inherent loss of accuracy.

With a knowledge of the velocity components, the surface position can be updated and the equation for the surface potential (4.3) can be integrated to complete the time step. In the next section we describe a procedure suitable for the numerical implementation of this technique.

6. Numerical implementation

The free surface is divided into N arcs. Cubic splines are used to interpolate between their end points. Cubic splines are also used to represent all the other variables pertaining to the free surface such as the potential, the vortex sheet strength, etc. At the boundaries of the computational domain, for some quantities, information is available on the value of the derivatives with respect to the arclength. For example, $\mathrm{d}r/\mathrm{d}s = 1$ and $\mathrm{d}z/\mathrm{d}s = 0$ on the axis of symmetry. In these cases such

information is used in the spline fitting. For other quantities, for which no such information is available, so called 'natural' spline conditions (i.e. vanishing of the second derivative with respect to the arclength) are imposed.

Starting with an initial guess for Γ, the integrals in (5.3a, b) are evaluated at each of the $N+1$ surface nodes. The values of ϕ_r^{m}, ϕ_z^{m} thus obtained are substituted into (5.4), a new value of Γ is generated, and so on iteratively. For integration in time, a second-order-accurate predictor-corrector method based on the trapezoidal rule is used. Under-relaxation with a weight of $\frac{1}{2}$ is used in the iteration procedure to help dampen the unstable behaviour of the surface.

In translating the above formulation into a numerical code we have the vectorizing capability of the supercomputer in mind. In the calculation, most of the computational work goes into the evaluation of the $2(N+1)^2$ integrals that arise when (5.3a, b) are evaluated at the surface nodes. It is therefore important to vectorize this step. This objective cannot be achieved if an adaptive Gaussian integration technique such as that used by Dommermuth *et al.* (1988) is followed. The use of a fixed number of Gaussian points, however, renders a full vectorization of the calculation of the integrals possible. Specifically, by use of the cubic-spline interpolation, we first evaluate at the Gaussian points the integrands that contain numerical data pertaining to the nodes such as Γ, r, and z and save them in an array. Later, when the integrals need to be evaluated at the different surface nodes, only the elliptic integrals require point-by-point evaluation. An analytical expression is used for this purpose and therefore all the integrals can be evaluated independently from each other in a vectorized fashion. In our program approximately 90% of the total CPU time is spent in simple vectorized DO-loops of this type. A standard practice in the evaluation of elliptic integrals is the removal of the logarithmic singularity. Although we followed this procedure in a first version of the code, we found that a straightforward Gaussian integration that ignores the weak logarithmic singularity performed just as well. This circumstance is in marked contrast to the simpler approach of earlier papers (Guerri, Lucca & Prosperetti 1982; Blake, Taib & Doherty 1986, 1987; Oğuz & Prosperetti 1989) in which the singularity had to be handled accurately. Ten Gaussian points in each arc of the free surface have been used in the results to be shown below.

Some form of smoothing of the free surface is a common practice in boundary-integral calculations and almost all of the examples available in the literature use some such technique, for example the five-point formula of Longuet-Higgins & Cokelet (1976), regridding (Dommermuth & Yue 1987), and others. In these calculations the effect of surface tension was neglected and the stability problem was modest. Here, however, since surface tension actually plays a crucial role in the physics of the process, it is imperative to use some kind of smoothing. In a first attempt, the regridding procedure introduced by Lin (1984) and used by Dommermuth & Yue (1987) was applied at each time step. This was found not to be sufficient, however. After many unsuccessful attempts we finally developed two new techniques.

Conceptually, the first one can be described as follows. One starts with nodes placed at equal distances from each other, the first node being on the axis of symmetry. When the new position of these nodes has been obtained, the total length of the computational free surface is calculated and a desirable interval Δs between two successive nodes is established. The node on the axis of symmetry is then again retained as the first node. However, the second node is placed at a distance $\frac{1}{2}\Delta s$ along the free surface from it, while all the other nodes follow at a distance Δs from each

other. The next-to-the-last node will then be at a distance $\frac{1}{2}\Delta s$ from the last node. At the next time step the half-interval adjacent to the axis of symmetry is eliminated and the regridding is done so that all nodes are at the same distance from each other. At the following time step, the second node is again put at $\frac{1}{2}\Delta s$ from the axis, and so on. This approach is similar in spirit to the use of staggered grids and its effectiveness is probably due to the same reason. In the actual implementation, it is desirable to use a slowly increasing spacing to extend the computational domain, but the essential concept remains the same.

The second technique is a curvature damping method that also is most effective at short wavelengths, where the stability problem is most severe. The technique is as follows. At each surface node the sign of the product $\mathscr{C}\,\mathrm{d}\mathscr{C}/\mathrm{d}t$ is examined. If the product is negative, nothing is done. If the product is positive, however, the evolution equation for the surface potential (4.3) is modified by the addition of a term proportional to $\mathrm{d}\mathscr{C}/\mathrm{d}t$,

$$\left.\frac{\mathrm{d}\phi}{\mathrm{d}t}\right|_S = \tfrac{1}{2}|\nabla\phi|^2 + \frac{1}{2Fr}z + \frac{2}{We}\left(\mathscr{C} + \lambda\frac{\mathrm{d}\mathscr{C}}{\mathrm{d}t}\right). \tag{6.1}$$

Values of λ ranging between 0.2 and 0.8 have been found to be adequate to stabilize the calculation while retaining a more than acceptable accuracy. Physically, this procedure may be interpreted as a sort of 'surface viscosity' which opposes the growth, but not the decrease, of the local surface curvature. This keeps the free surface smooth, especially in the initial stages of the impact where the instability is almost pathological. In most of the cases that we have calculated we have found the two smoothing procedures to work equally well.

7. Initial conditions

The initial shape of the free surface that is assumed in this calculation is shown in the first frame of figures 2(*b*) and 3(*b*). Ideally, this shape should be that of a sphere tangent to the plane surface. As was shown in Oğuz & Prosperetti (1989), in the initial stages of the impact, contact between the surfaces of the drop and of the receiving liquid occurs at a number of points. This circumstance gives rise to a vortex sheet separating the drop material from that of the underlying liquid. We have carried out calculations, to be described elsewhere, that show that this vortex sheet is very weak and has a negligible influence on the process. Since its inclusion would greatly complicate the present calculation, we have chosen to ignore it and we believe that the extent to which our numerical results match the experimental ones justifies this procedure. However, this approach requires that the calculation be started with the two liquids already in contact over a finite area. We show in figure 5 the free-surface configuration at the moment of bubble entrapment as calculated starting with two different initial conditions for the case of figure 2. For the first calculation the contact between the surfaces of the drop and of the receiving liquid extends over an area corresponding to a solid angle of 0.65 rad, in the second example of 1.0 rad. It can be seen that the final results are only slightly affected by the precise form of this initial condition.

Although a smaller amount of free surface would presumably be destroyed in lower-velocity than in higher-velocity impacts, to avoid arbitrariness we have used the same initial configuration for all of our simulations.

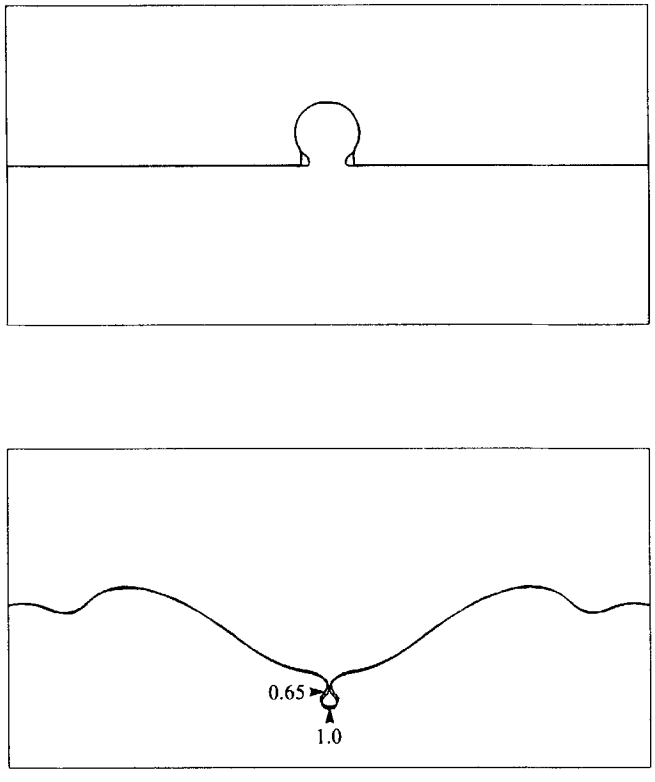

FIGURE 5. The effect of initial configuration on the configuration of the free surface at the moment of bubble entrapment for the case of figure 2, $R = 1.9$ mm, $U = 1.53$ m/s. The two cases differ in the amount of surface area over which contact is established at $t = 0$, which is equivalent to an opening angle of 1 and 0.65 rad.

8. Comparison between experiment and numerical results

The impact cases that will be discussed in detail in this section are indicated by the letters A–J in the (R, U)-plane of figure 6. This is the same as figure 1 with only the best fits to the lower and upper bubble boundaries shown.

We begin by considering the two cases $R = 1.9$ mm, $U = 1.534$ m/s, and $R = 2.9$ mm, $U = 2.40$ m/s for which Pumphrey & Crum (1988) publish detailed photographic sequences reproduced here in figures 2(*a*) and 3(*a*) respectively. The first case corresponds to the point marked J in the (U, R)-plane of figure 6, while the second case is out of scale. A bubble is entrained in the first instance, while in the second one the typical, nearly hemispherical crater shape is observed.

We juxtapose in figures 2(*a*) and 2(*b*) the experimental and the numerical surface shapes at comparable times for the first case. The most salient discrepancy between calculation and experiment is the surface ripple at the edge of the crater which is not visible in the photographic results. In judging the importance of this difference it should be kept in mind that the movie has been taken at a slight angle below the free surface, a circumstance that would render the presence of a small ripple undetectable. Whether this factor is enough to explain this discrepancy is not clear. At least in part, this discrepancy may be due to the rather crude way in which the initial conditions for the calculations are set. In spite of this difference, however, the general shape and

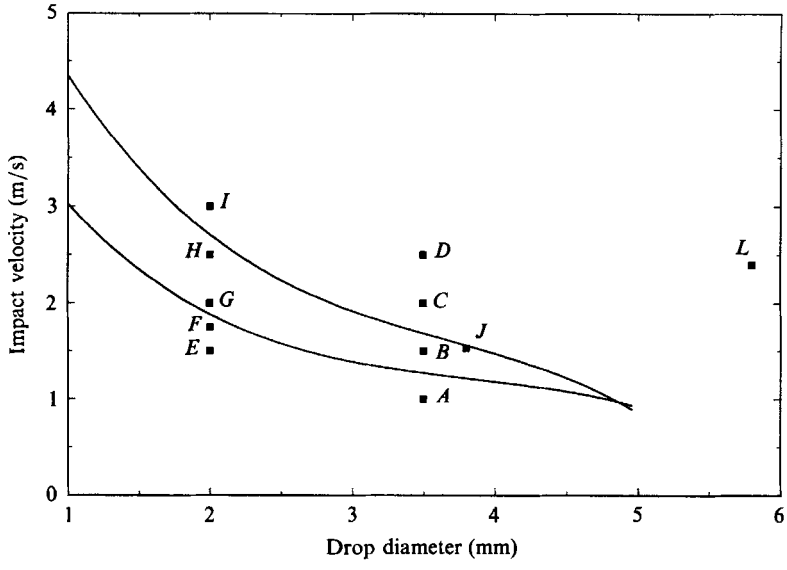

FIGURE 6. Bubble boundaries from figure 1 in the (R, U)-plane. The letters indicate the cases simulated numerically and discussed in detail in §8. The cases A, B, C, D are shown in figure 9; E, F, G, H, I in figure 11, J in figure 2 and L in figure 3.

aspect ratio of the crater compares well with the calculation. A second discrepancy is in the time to experimental and theoretical bubble entrapment, which in our dimensionless units $t_* = Ut/R$ is 21.1 and 23.0 respectively. Although again part of this difference may be due to the various approximations made, it may also be noted that there is an uncertainty in the experimental value of both the time at which contact between the drop and the receiving liquid is established and the time at which a closed bubble is formed. At 1000 frames per second, for this case, the interval between two frames is about 1.2 dimensionless time units which is sufficient to account for the observed difference. We feel that, with due consideration of these factors, agreement between theory and experiment is quite good and lends substantial support to our model and calculational procedure. A different view of the free surface for this case, affording a better appreciation of the three-dimensional nature of the process, is shown in figure 7.

We present an analogous comparison for the second case, $R = 2.9$ mm, $U = 2.40$ m/s, in figure 3. Contrary to the previous case, a thin three-dimensional splash appears almost immediately. It is clear that the numerical method does a rather poor job at reproducing this feature. The computed splash is much thicker and, perhaps as a consequence of this, much less inclined outward. However, compared with the computed splash of the previous case, it appears to be substantially thinner so that this trend at least is reproduced by the calculation. Here the problem may in part be one of resolution, although it is doubtful that features on such a small scale can be reproduced by the present numerical method while maintaining an acceptable stability of the algorithm. In any case, we have not attempted to obtain such a resolution. The photos also show much more pronounced capillary waves than the calculation. Evidently, this difference is part of the price paid to achieve stability. With these exceptions, the calculations do, however, compare very well with the photographs. The time evolution is closely mirrored by the calculation up to the jet

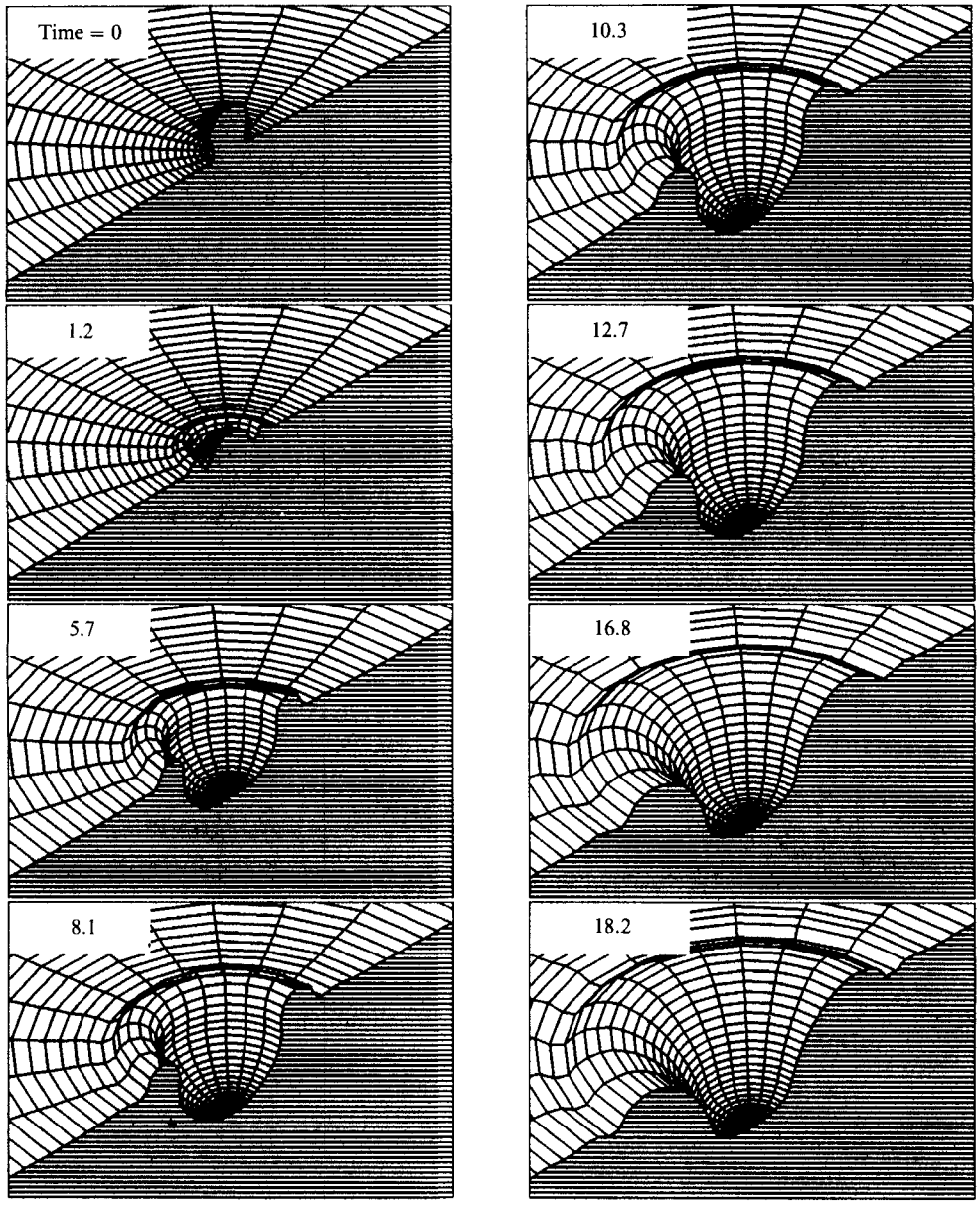

FIGURE 7. For caption see facing page.

rising from the centre of the crater and a secondary drop pinching off from its tip. It may be remarked that the small structure visible in the frames at times $t_* = 32.5$ and 36.7 is produced by the impact of a small satellite drop trailing behind the main one that impacted at time 0.

A more detailed view of the central part of this calculation is shown in figure 8. In this case the regridding procedure has proven inadequate to stabilize capillary effects in the neighbourhood of the axis of symmetry after a dimensionless time around 50. The problem is that the capillary wave that travels toward the axis of symmetry (see e.g. the panel for $t_* = 50.526$ in figure 3*b*) becomes too large as it gets closer to it

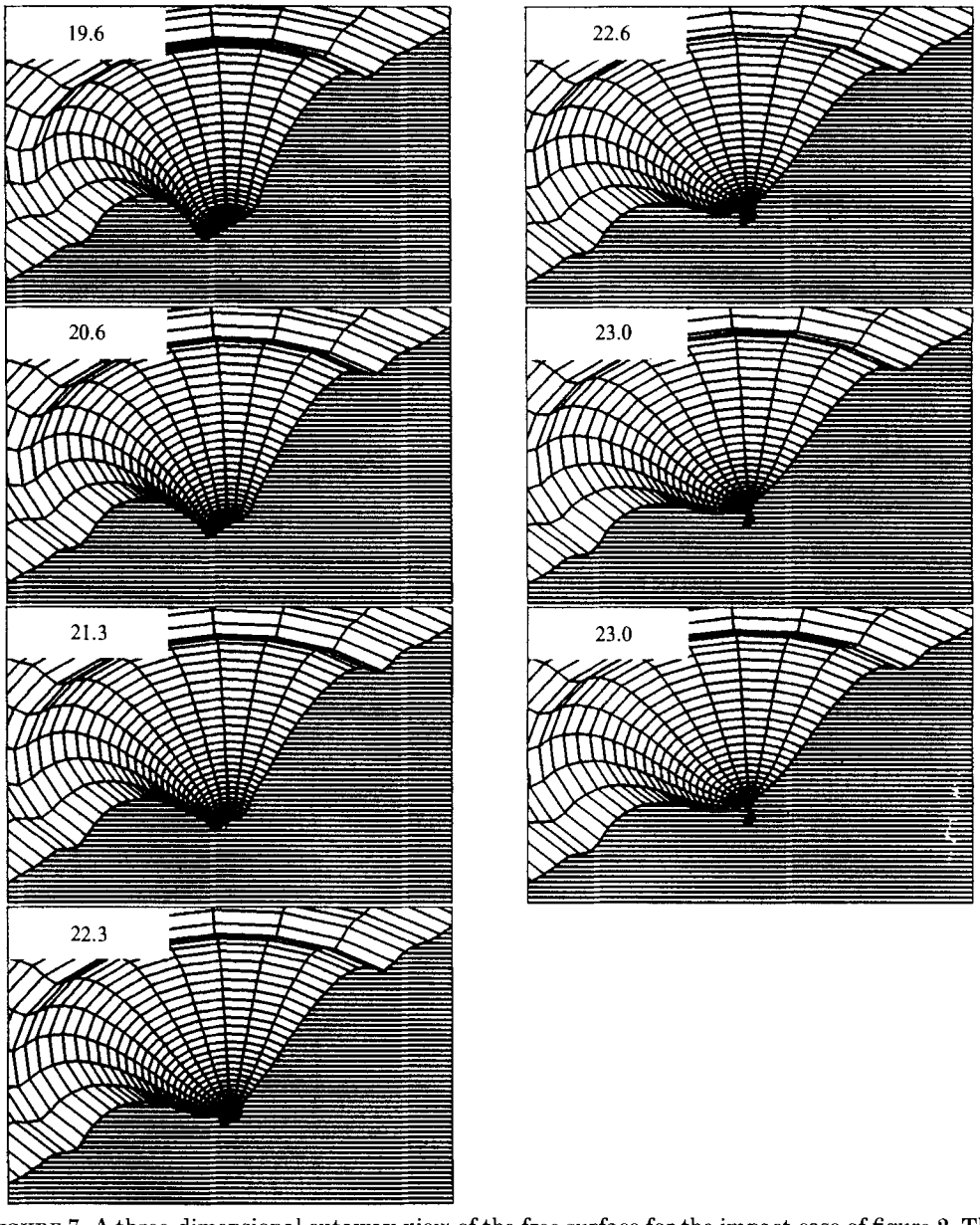

FIGURE 7. A three-dimensional cutaway view of the free surface for the impact case of figure 2. The times indicated in the upper left-hand corner of each frame are non-dimensional values of the quantity $t_* = Ut/R$. In this case the reference time is $R/U = 1.2$ ms.

and destroys the calculation. In this case it has been necessary to use an additional damping for a short interval of time between dimensionless times 47 and 56 approximately. The five-point formula of Lundgren & Mansour (1988) has been used for this purpose.

We have carried out a number of other simulations for various drop radii and impact velocities. In figure 9(*a–d*) we present results for $R = 1.75$ mm and impact velocities of 1, 1.5, 2, and 2.5 m/s. These cases correspond to the points marked A, B, C, D in the (R, U)-plane of figure 6.

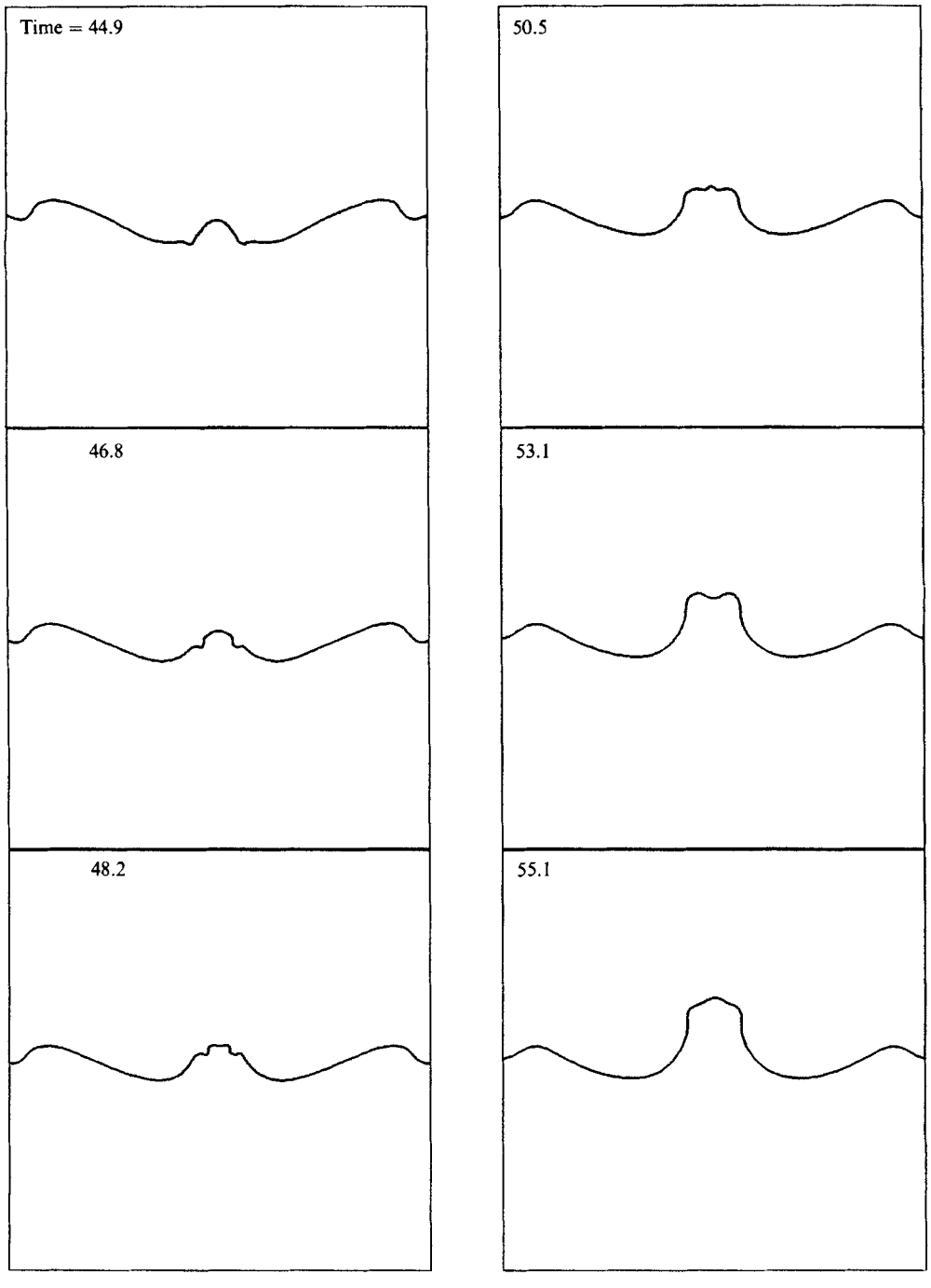

FIGURE 8. For caption see facing page.

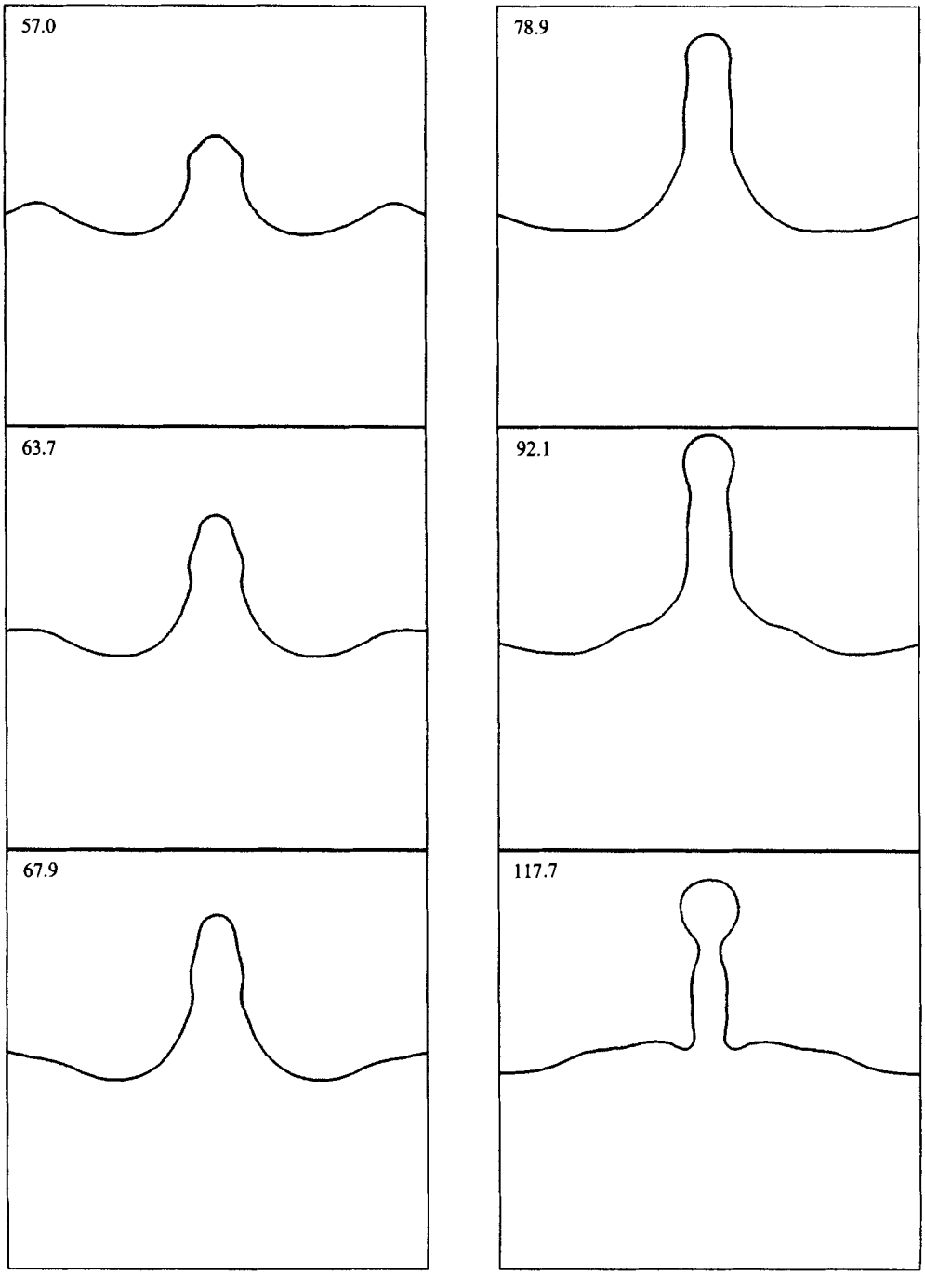

FIGURE 8. A more detailed sequence of the free-surface evolution between the last two frames of figure 3.

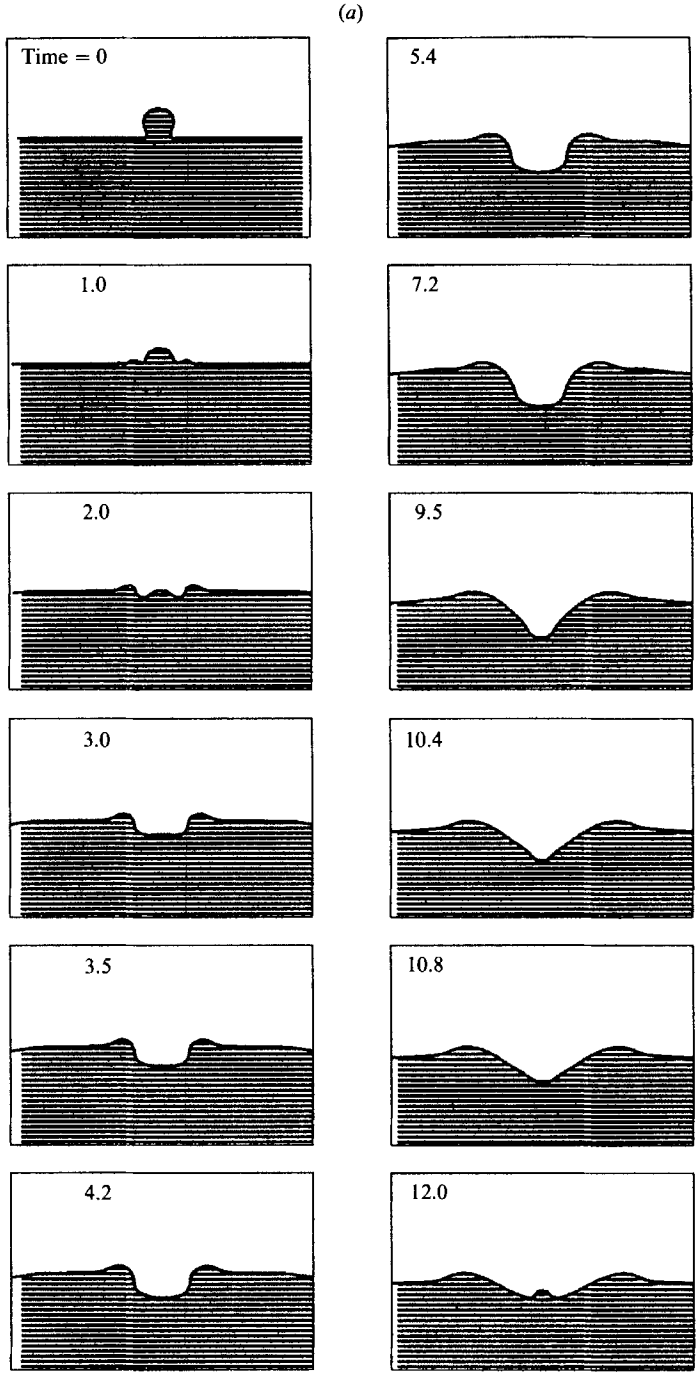

FIGURE 9(a). For caption see p. 167.

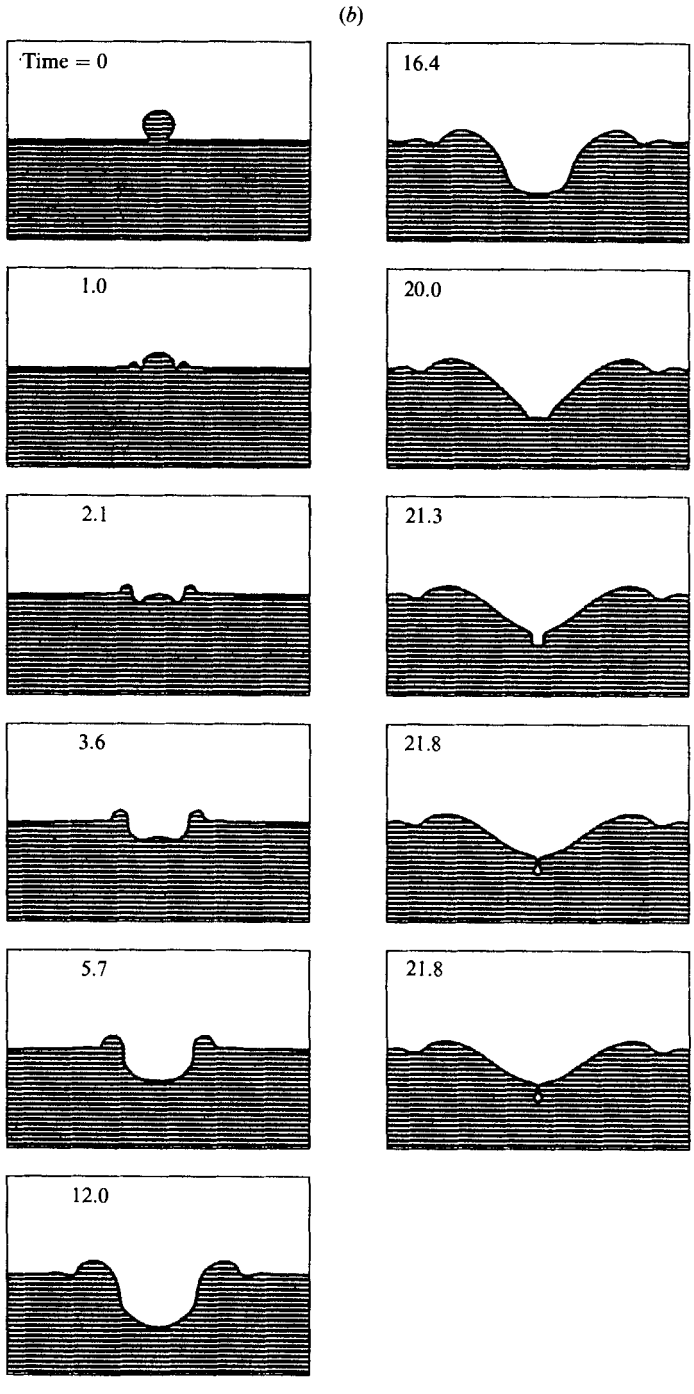

FIGURE 9(*b*). For caption see p. 167.

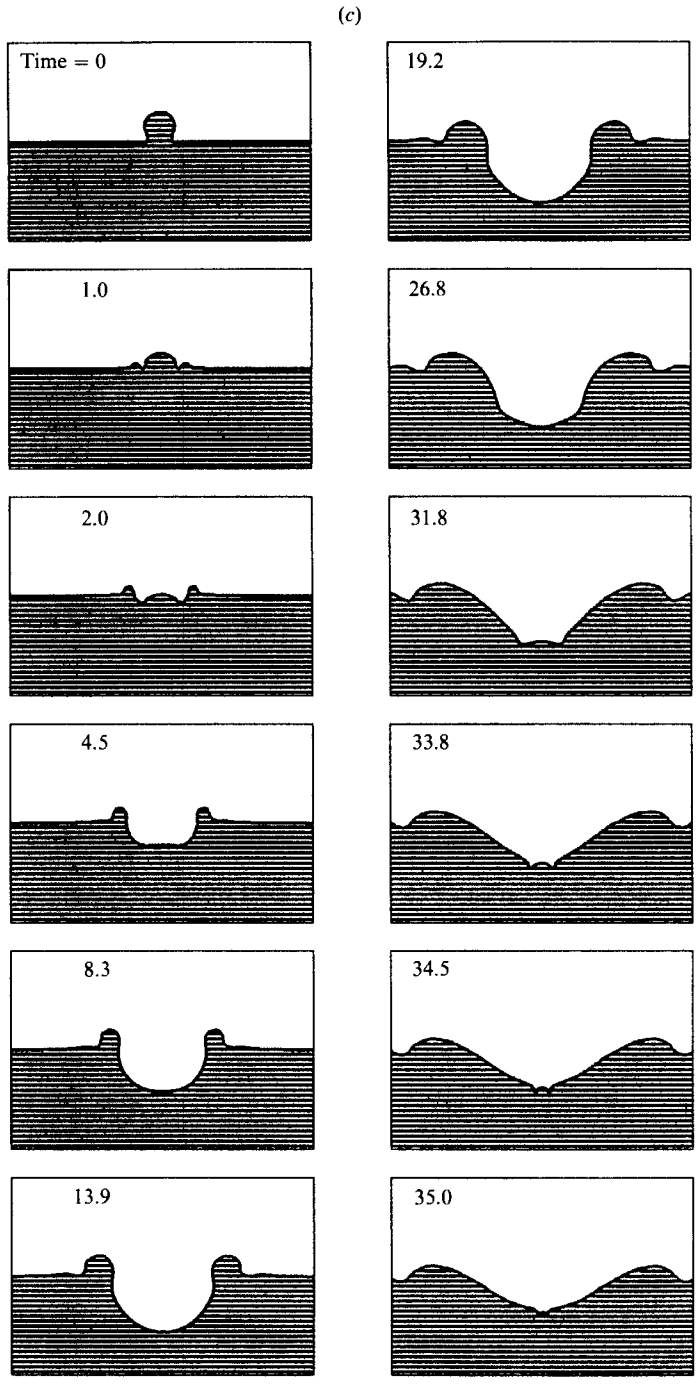

FIGURE 9(c). For caption see facing page.

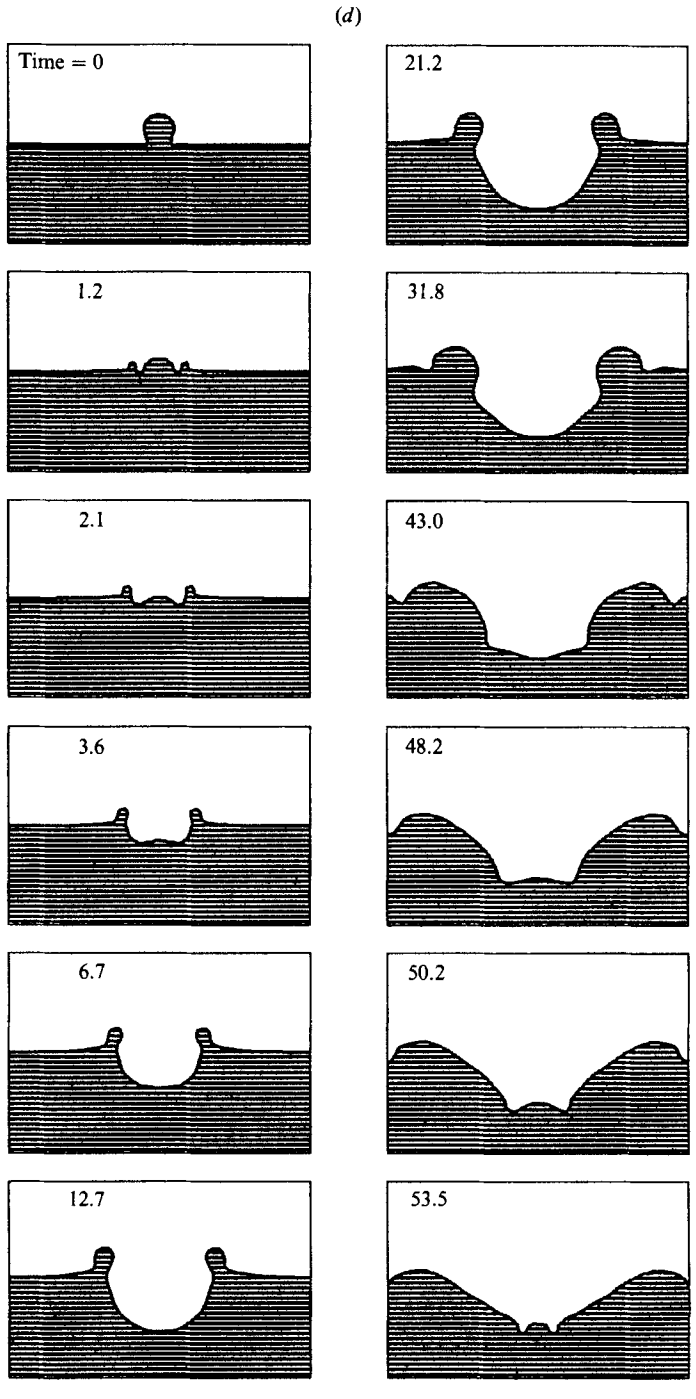

FIGURE 9. Successive computed surface shapes of a drop impacting a plane surface for $R = 1.75$ mm and (*a*) $U = 1$ m/s, (*b*) 1.5 m/s, (*c*) 2 m/s, (*d*) 2.5 m/s. These cases correspond to the points marked *A*, *B*, *C*, *D* in figure 6. The times indicated are non-dimensional values of the quantity $t_* = Ut/R$.

At the lowest impact velocity ($U = 1$ m/s, figure 9*a*) the crater is too shallow to trap a bubble. The drop is seen to penetrate into the liquid almost undeformed and its top can be followed up to a depth of about one radius. At this moment the shape of the crater is nearly rectangular. This behaviour is observed in almost all the cases considered here. This initial rectangular shape evolves into a more rounded one and when maximum depth is reached the crater takes on a characteristic conical shape. After this, it starts filling up from the bottom before any bubble can remain entrapped. This is consistent with the experimental findings of figure 1. Owing to the high surface-tension effect, in this case hardly any jet is formed as the crater fills up. The net effect of the impact is therefore to produce a surface ripple.

According to figure 6, the next case ($U = 1.5$ m/s, figure 9*b*) lies on the boundary of the bubble region and the numerical results show that a bubble is entrained. A comparison with the previous case shows a deeper crater, a longer timescale, and the characteristic 'nipple' which is ultimately responsible for the formation of the bubble. The last two cases ($U = 2$ and 2.5 m/s, figures 9*c* and 9*d*) are above the bubble region and the crater fills with a jet from the bottom. A more spherical shape and the presence of large capillary waves in the crater are prominent differences with the previous two cases.

For a fixed radius, increasing the velocity of impact has the effect of increasing the Froude number and decreasing the Weber number. The gradually more prominent ridge around the rim of the crater that is observed in going through the previous sequence is a consequence of this weakening of surface-tension forces with respect to gravitational and inertial effects. In all these examples the computational domain is three times as big as the frames shown and the duration of the calculation is short enough that no boundary effects arise from the truncation of the domain. One may also note the scaling of the duration of the process with a power of U greater than 1, as already mentioned in §3.

It is instructive to compare, see figure 10, the last three computed surface configurations for the cases of figures 9(*b*), 9(*c*), 9(*d*). The disappearance of bubble entrapment in going from figure 9(*b*) to 9(*c*) and then to 9(*d*) is seen to be due essentially to the difference in the times at which the sides and the bottom of the crater invert their motion. For the bubble to be entrapped, the bottom of the crater is still moving downward when the sides have already started to move inward. As the impact velocity increases, the inward motion of the sides starts later and later until, in the last case, it has not yet begun at the moment at which the bottom starts to fill up with a jet. The marginal case captured in figure 10(*b*) is that in which essentially the bottom jet has grown just enough to fill up the space enclosed between the sides. The detailed timing of these processes explains why the entrapment of bubbles by a falling drop is such an improbable event.

A sequence similar to that of figure 9 is shown in figure 11(*a–e*) for $R = 1$ mm and $U = 1.5$, 1.75, 2, 2.4, and 3 m/s. These cases are marked by the points *E*, *F*, *G*, *H*, *I* in figure 6. The first case shows a behaviour very similar to the lowest velocity case of the previous sequence. The second case is very near, but outside, the lower bubble boundary. Here a bubble is not trapped because the motion of the bottom of the crater inverts too late, but nevertheless conditions are so close to the entrapment of a bubble that the characteristic 'nipple' forms. This region of large curvature causes a very low pressure in the liquid, which gives origin to a thin jet. The last three frames show the tendency of the tip of this jet to break off owing to a capillary instability.

The next case, figure 11(*c*), is just inside the bubble region. It can be seen here that

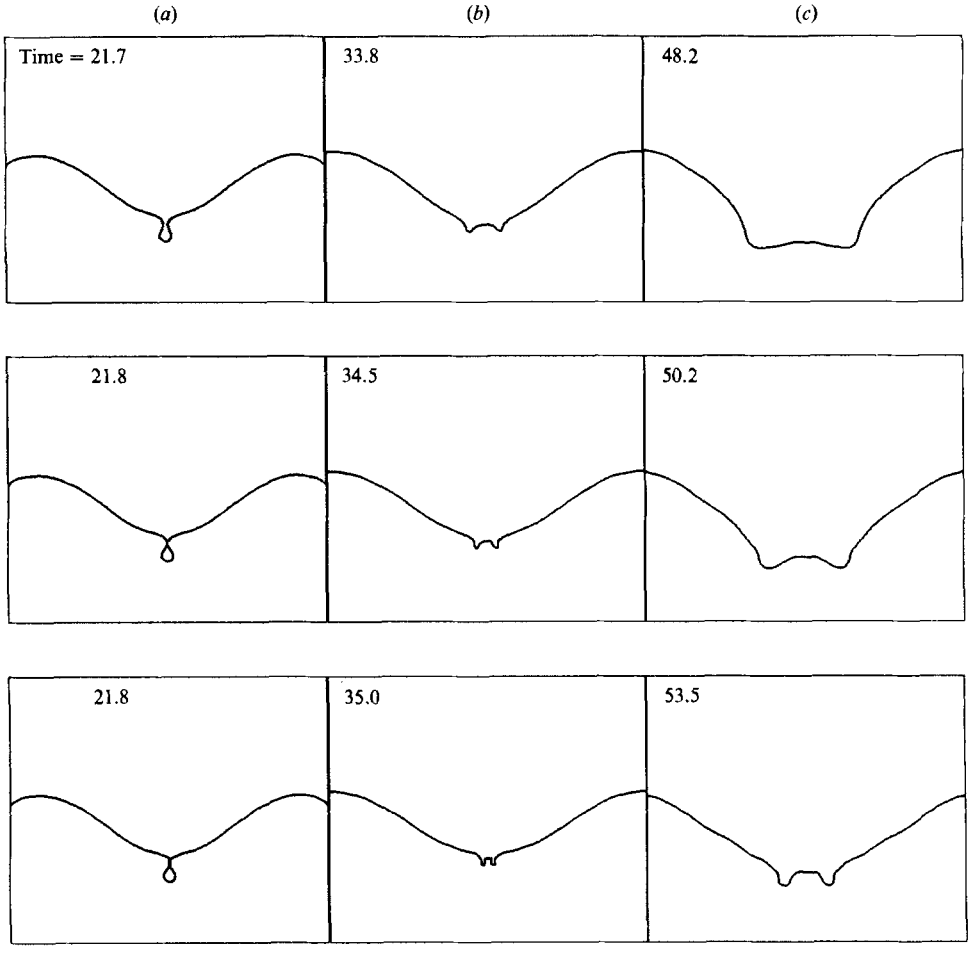

FIGURE 10. Last three computed shapes of the free surface for an impacting drop of radius 1.75 mm at three different velocities. The first row corresponds to $U = 1.5$ m/s (figure 9*b*), the second to $U = 2$ m/s (figure 9*c*) and the third to $U = 2.5$ m/s (figure 9*d*). The non-dimensional time is indicated in the upper left corner of each frame. The width of each frame is 20 times the radius of the impacting drop.

the mechanics of the process is such that, right on the boundary, the volume of the entrapped bubble is not zero but has some finite value. In other words, as the boundary is approached from the outside, the 'nipple' at the bottom of the crater shows a greater and greater tendency to close off. Right at the boundary, therefore, a bubble is entrapped having essentially the volume of the nipple. As one penetrates deeper into the bubble region, as in figure 11(*d*), the volume of the bubble becomes larger, but not more than a few times than at the point of incipient formation. This remark has some important implications for the noise produced by rain falling on bodies of water, as will be mentioned in the next section (see also Prosperetti *et al.* 1989). Finally, the high-impact-velocity case of figure 11(*e*) shows a behaviour very similar to that seen earlier in figure 9(*d*).

The apparent proportionality of the crater growth time to $U^{\frac{1}{3}}$ has already been mentioned in §3. We show in figure 12 a comparison between this experimentally based relation and the computed dimensionless time to achieve minimum kinetic

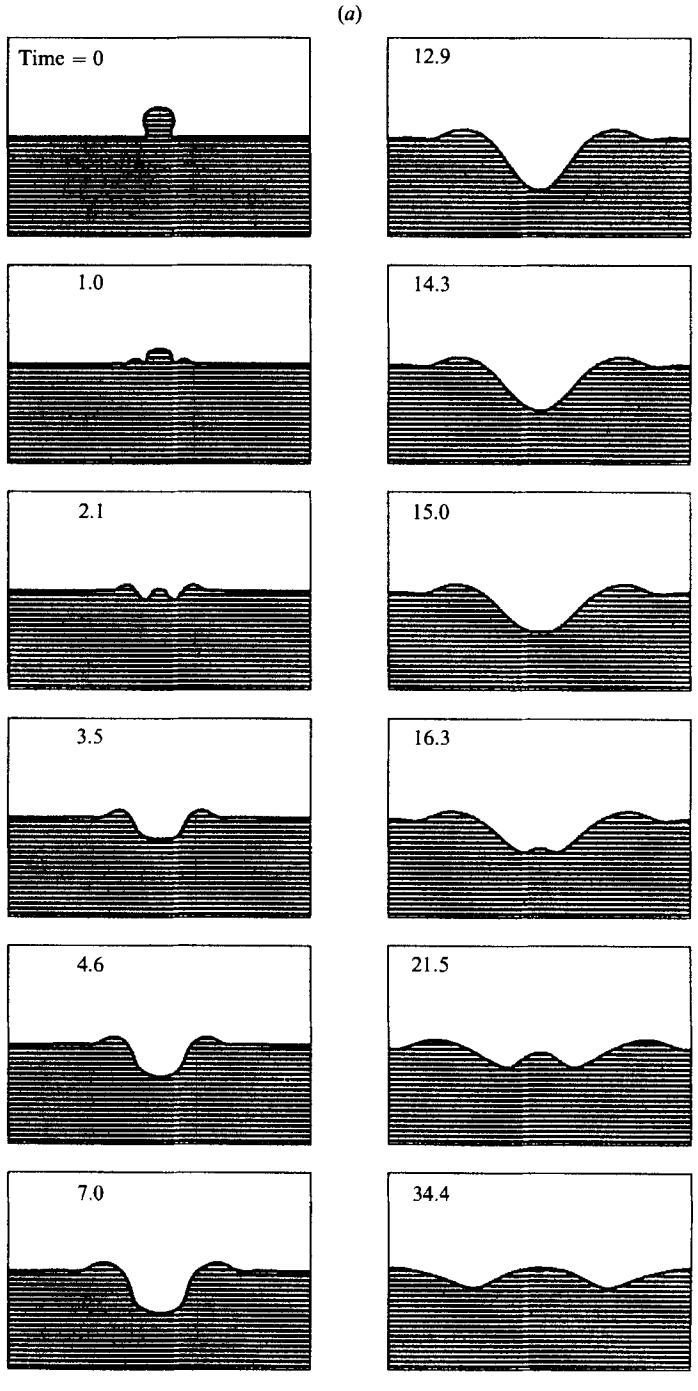

FIGURE 11(a). For caption see p. 174.

(*b*)

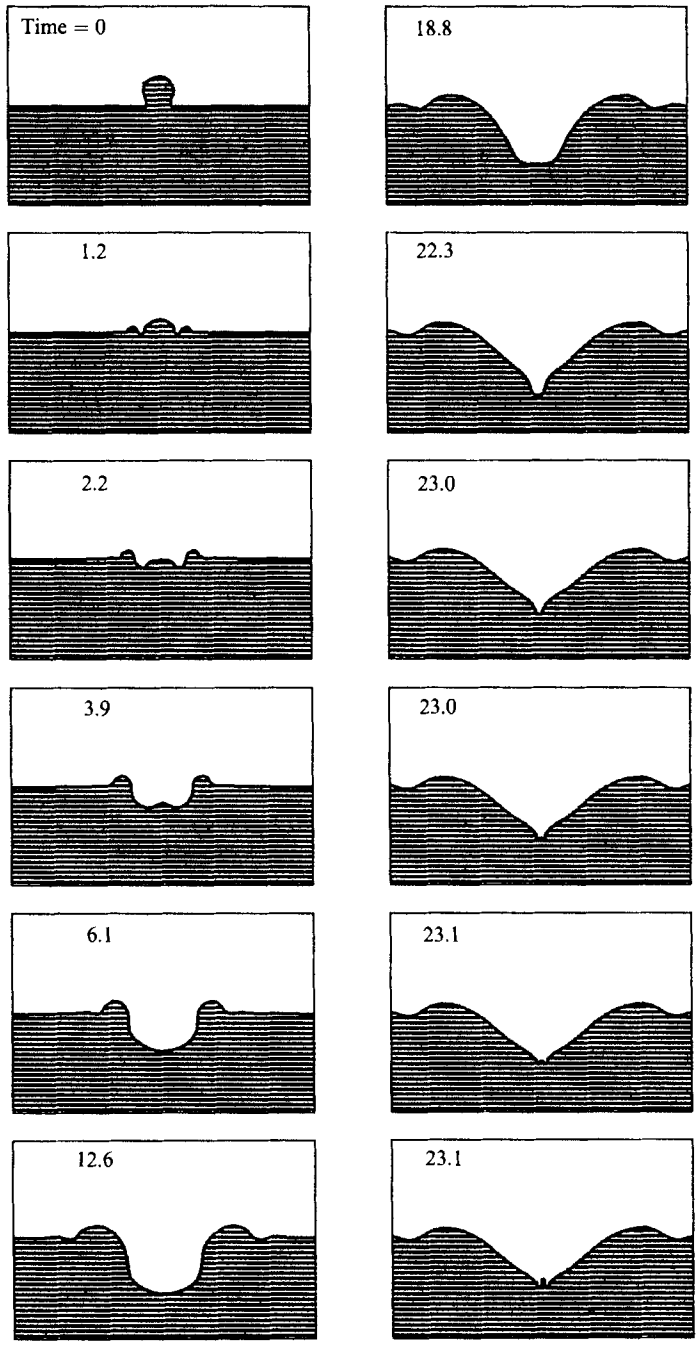

FIGURE 11(*b*). For caption see p. 174.

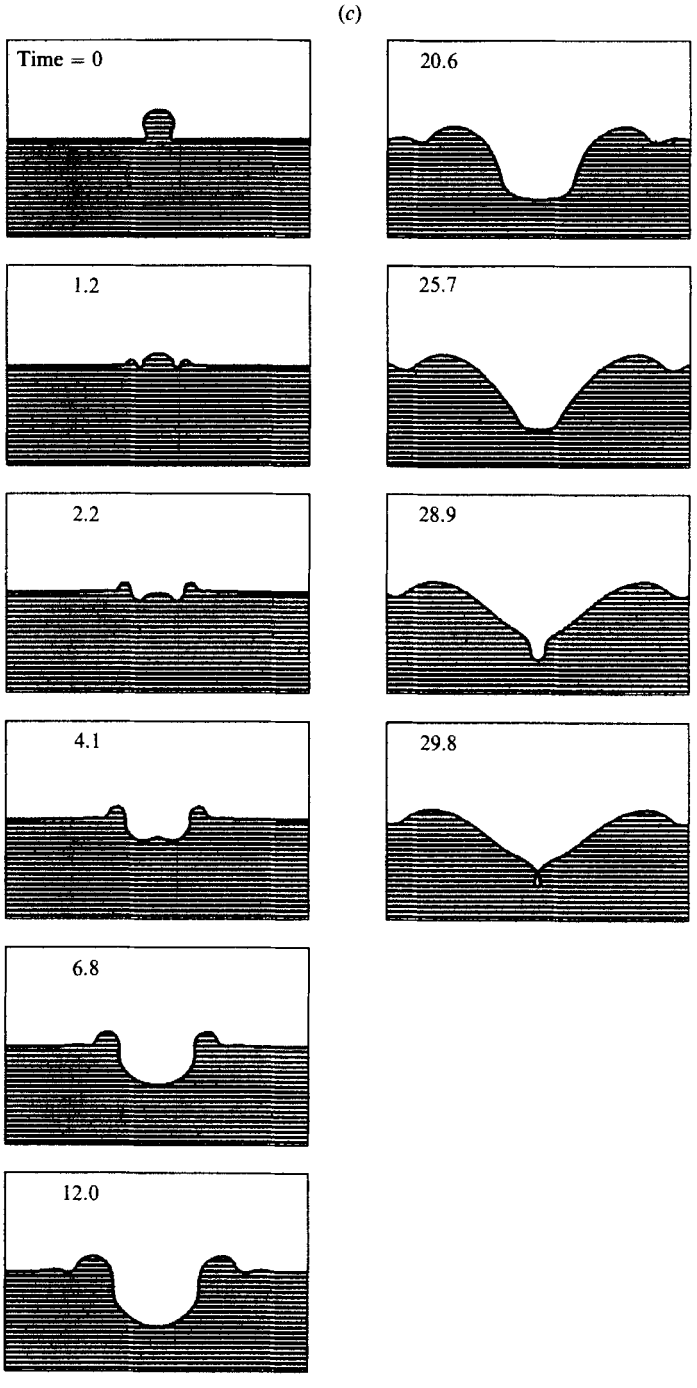

FIGURE 11(c). For caption see p. 174.

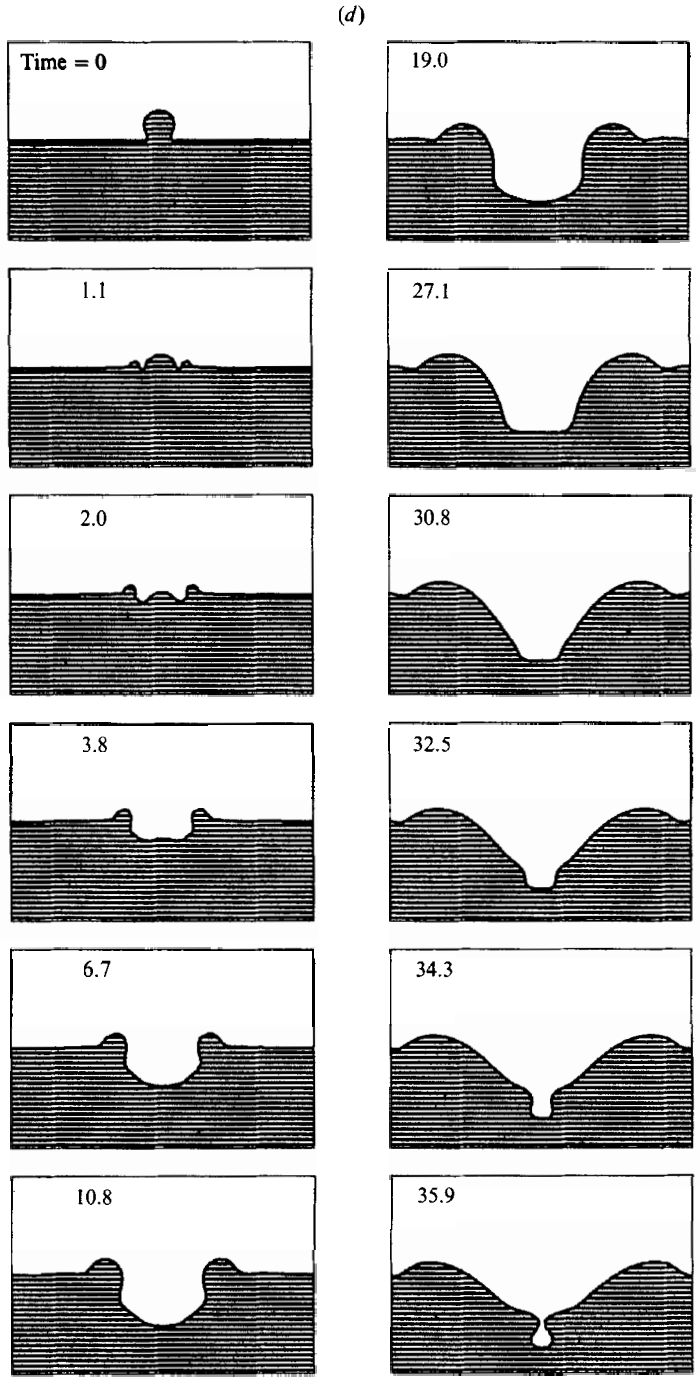

FIGURE 11 (*d*). For caption see next page.

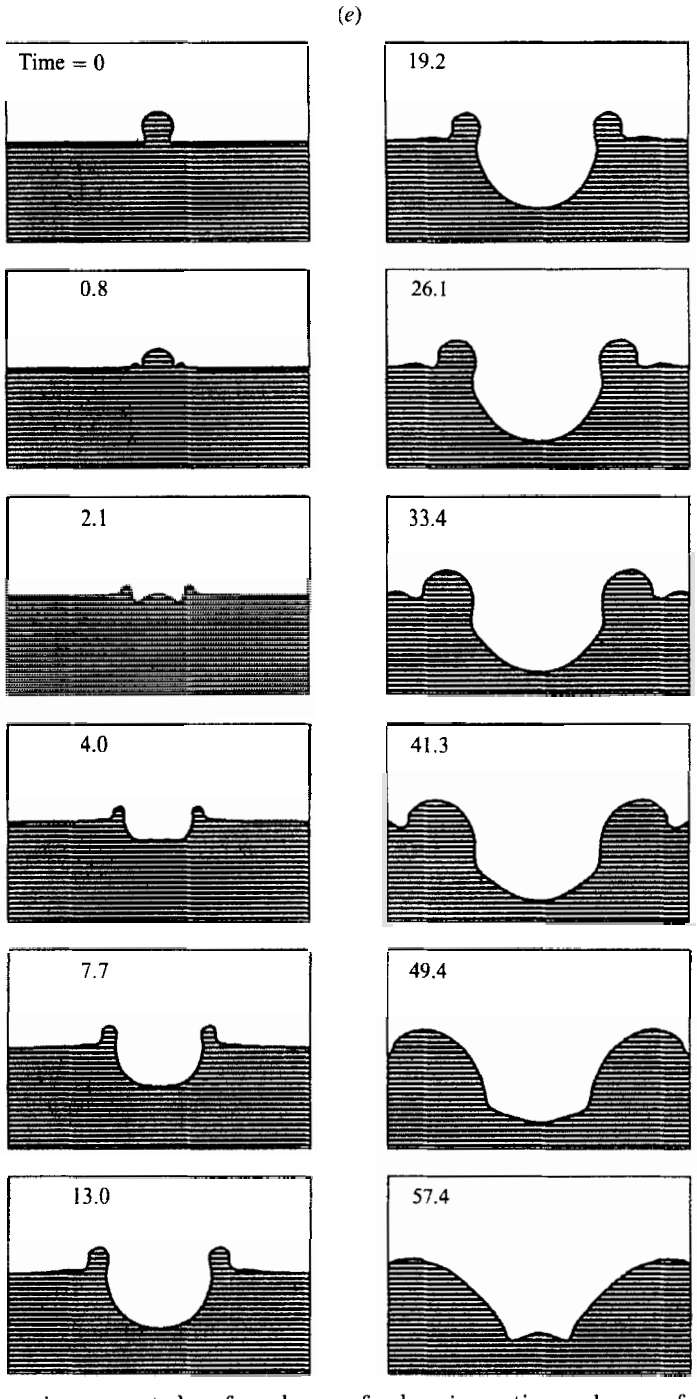

FIGURE 11. Successive computed surface shapes of a drop impacting a plane surface for $R = 1$ mm and (*a*) $U = 1.5$ m/s, (*b*) 1.75 m/s, (*c*) 2 m/s, (*d*) 2.4 m/s, and (*e*) 3 m/s. These cases correspond to the points marked E, F, G, H, I in figure 6. The times indicated are non-dimensional values of the quantity $t_* = Ut/R$.

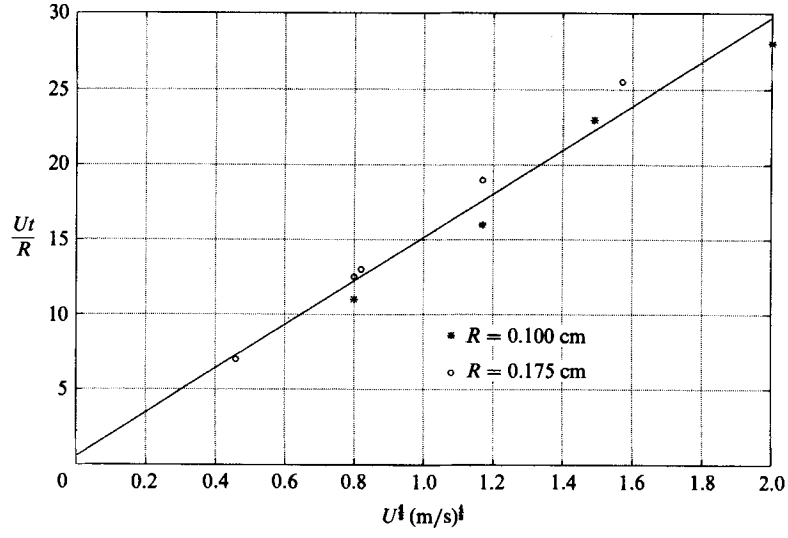

FIGURE 12. The dimensionless time to minimum kinetic energy is shown versus $U^{\frac{1}{2}}$. According to the data, the relationship should be the straight line shown.

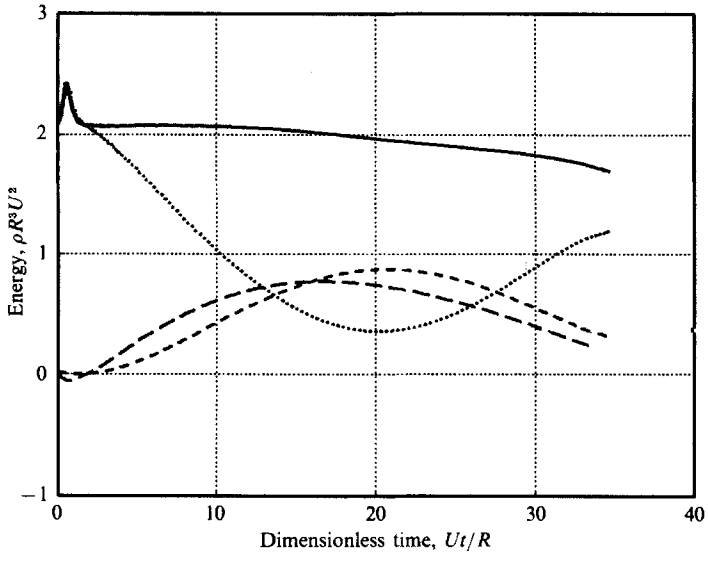

FIGURE 13. Dimensionless energy versus dimensionless time for the case of figure 9(*c*), $R = 1.75$ mm, $U = 2$ m/s. The solid line is the total energy, the dotted line is the kinetic energy, the short-dashed line is the gravitational potential energy, and the long-dashed line is the surface-tension energy calculated as explained in the text.

energy for two different values of the radius. The agreement is, also in this case, quite good.

Finally, we show in figure 13 the dimensionless energy versus time for a typical case, that of figure 9(*c*). The energy is expressed in units of $\rho R^3 U^2$, which renders the initial value equal to $\frac{2}{3}\pi \approx 2.094$. At time zero the gravitational potential energy associated with the drop position is included but the surface energy is taken to vanish to avoid the inclusion of a large constant that would have obscured the performance of the numerical method. At any subsequent time the surface energy is evaluated by

subtracting from the total area the total initial area consisting of the undisturbed plane surface plus the surface of the impacting droplet. The figure shows the total energy to remain very nearly constant. The most serious irregularities are found for small times where the precision of the calculation is reduced by the rather crude initial condition. Later on the curves look relatively smooth with a residual waviness due to capillary waves. It can be seen that the oscillations of the kinetic and surface-tension energies have opposite phases, which indicates an exchange between these two forms of energy which is not necessarily the result of numerical inaccuracies but could very well occur in nature.

9. Discussion

We have presented a qualitative and a computational analysis of the process by which impacting liquid drops are able to entrap bubbles at the bottom of the crater that they form on the surface of a liquid. We have found that whether a bubble is entrapped or not is determined by a delicate balance between the times at which the outward motion of the crater walls is reversed at different positions. In this sense, bubble entrapment may be considered an event with relatively low probability.

An interesting finding is that the fluid mechanics of the process is such that bubbles entrapped in marginal conditions do not have a vanishingly small volume. Rather, bubbles entrapped near the boundaries of the bubble region have a size comparable with that of bubbles formed well within the bubble region. As a result, not much variation in the size of bubbles entrapped by droplets of the same radius impacting at different velocities is observed. As shown by Prosperetti *et al.* (1989), this feature is responsible for the peculiar underwater acoustic signature of rain. Indeed, rain drops impinge at terminal velocity so that a functional relationship exists between their radius and impact velocity. It turns out that this relation, represented by the dashed line in figure 1, has a very large slope so that bubble-entraining droplets have radii in a very narrow size range, from 0.450 to 0.475 mm, approximately, and a correspondingly narrow range in impact velocities, from 3.66 to 3.84 m/s. The bubbles entrained by rain will therefore also have a very narrow spread in radii. Hence if, as experiment suggests (Pumphrey & Crum 1988; Pumphrey *et al.* 1989), only bubble-entrapping drops contribute to the underwater noise of rain, one would expect this noise to exhibit a peak at a rather well-defined frequency, corresponding to the natural frequency of the entrained bubbles. This is precisely what is observed experimentally (Scrimger 1985; Scrimger *et al.* 1987; Scrimger, Evans & Lee 1989; Prosperetti *et al.* 1989), with the peak around 14–15 kHz. While we shall present detailed calculations lending further support to this hypothesis in a separate publication, we remark here that our computations estimate the radii of the bubbles entrained by drops to be between 0.19 and 0.30 mm. The natural frequencies of these bubbles span the range between 11 and 17 kHz, the centre frequency of which coincides with the position of the characteristic spectral peak of rain noise.

The authors would like to express their gratitude to Professor L. A. Crum and Dr H. C. Pumphrey for sharing with them so liberally their experimental observations, data and photographs. We wish also to thank Dr G. Chahine for taking some high-speed movies of the impact of coloured drops and showing them to us. This study has been supported by the Ocean Acoustics Branch of the Office of Naval Research.

Appendix

Since $\phi_r \cos\psi$ and ϕ_z, being the Cartesian components of the velocity field, are harmonic, in view of the axial symmetry, we can write the following Green's identities in the cylindrical coordinate system (z, r, ψ):

$$\phi_z = \frac{1}{4\pi}\int_S \phi_{zn}\left(\int_0^{2\pi}\frac{1}{\rho}\,\mathrm{d}\psi\right) r\,\mathrm{d}s - \frac{1}{4\pi}\int_S \phi_z \frac{\partial}{\partial n}\left(\int_0^{2\pi}\frac{1}{\rho}\,\mathrm{d}\psi\right) r\,\mathrm{d}s \tag{A 1}$$

and

$$\phi_r = \frac{1}{4\pi}\int_S \phi_{rn}\left(\int_0^{2\pi}\frac{\cos\psi}{\rho}\,\mathrm{d}\psi\right) r\,\mathrm{d}s - \frac{1}{4\pi}\int_S \phi_r \frac{\partial}{\partial n}\left(\int_0^{2\pi}\frac{\cos\psi}{\rho}\,\mathrm{d}\psi\right) r\,\mathrm{d}s, \tag{A 2}$$

where

$$\rho = (R - r\cos\psi)^2 + r^2\sin^2\psi + (Z-z)^2$$

is the distance between the field point $(Z, R, 0)$ and the field point (z, r, ψ). Here the subscripts z, r, n denote partial differentiation. With our choice that the arclength s is zero on the axis of symmetry, the unit normal $\boldsymbol{n}$ and the unit tangent vector $\boldsymbol{t}$ are given by

$$\boldsymbol{n} = \left(\frac{\partial r}{\partial s}, -\frac{\partial z}{\partial s}\right), \quad \boldsymbol{t} = \left(\frac{\partial z}{\partial s}, \frac{\partial r}{\partial s}\right).$$

The form (A 1), (A 2) is not the most suitable one for numerical computation because it involves normal derivatives. Since, however, ϕ is harmonic, these derivatives can be expressed in terms of tangential ones using the relations

$$\phi_{zn} = -\frac{\partial z}{\partial s}\phi_{rz} + \frac{\partial r}{\partial s}\phi_{zz} = -\frac{\partial}{\partial s}\phi_r - \frac{\partial r}{\partial s}\frac{1}{r}\phi_r,$$

and

$$\phi_{rn} = -\frac{\partial z}{\partial s}\phi_{rr} + \frac{\partial r}{\partial s}\phi_{rz} = \frac{\partial}{\partial s}\phi_z + \frac{\partial z}{\partial s}\frac{1}{r}\phi_r,$$

which can now be evaluated with a knowledge of ϕ_r and ϕ_z on the surface.

The angular integrations in (A 1) and (A 2) can be carried out explicitly by the substitution $2\theta = \psi$. Indeed, we find

$$I_1 = \int_0^{2\pi}\frac{\mathrm{d}\psi}{\rho} = \frac{4}{A^{\frac{1}{2}}}\int_0^{\pi/2}\frac{\mathrm{d}\theta}{(1-m\cos^2\theta)^{\frac{1}{2}}},$$

$$I_2 = \int_0^{2\pi}\frac{\cos\psi}{\rho}\,\mathrm{d}\psi = \frac{4}{A^{\frac{1}{2}}}\int_0^{\pi/2}\frac{(2\cos^2\theta - 1)}{(1-m\cos^2\theta)^{\frac{1}{2}}}\,\mathrm{d}\theta,$$

where

$$A = (R+r)^2 + (Z-z)^2,$$

and m is given by

$$m = \frac{4rR}{A}.$$

Recalling the definition of the complete elliptic functions of the first and third kind of argument m,

$$K(m) = \int_0^{\pi/2}\frac{\mathrm{d}\theta}{(1-m\cos^2\theta)^{\frac{1}{2}}}$$

and

$$D(m) = \int_0^{\pi/2}\frac{\cos^2\theta}{(1-m\cos^2\theta)^{\frac{1}{2}}}\,\mathrm{d}\theta,$$

it is easily seen that substitution of I_1 and I_2 into the Green's identity evaluated on the surface with the limits

$$\tfrac{1}{2} = -\lim_{\delta\to 0}\frac{1}{\pi}\int_{-\delta}^{\delta}\frac{\partial}{\partial n}\frac{K}{A^{\frac{1}{2}}}r\,\mathrm{d}s,$$

and

$$\tfrac{1}{2} = -\lim_{\delta\to 0}\frac{1}{\pi}\int_{-\delta}^{\delta}\frac{\partial}{\partial n}\frac{2D-K}{A^{\frac{1}{2}}}r\,\mathrm{d}s,$$

gives (5.1 a, b) with the definitions

$$G = \frac{2r}{\pi}\frac{K(m)}{A^{\frac{1}{2}}}, \quad H = \frac{2r}{\pi}\frac{\partial}{\partial n}\frac{K(m)}{A^{\frac{1}{2}}},$$

$$F = \frac{2r}{\pi}\frac{2D(m)-K(m)}{A^{\frac{1}{2}}}, \quad E = \frac{2r}{\pi}\frac{\partial}{\partial n}\frac{2D(m)-K(m)}{A^{\frac{1}{2}}}.$$

Explicit expressions for the normal derivatives appearing in these formulae are

$$\frac{\partial}{\partial n}\frac{K(m)}{A^{\frac{1}{2}}} = \frac{1}{A^{\frac{1}{2}}}\left[\frac{\boldsymbol{h}\cdot\boldsymbol{n}}{B}E(m) - \frac{K(m)-E(m)}{2r}\hat{\boldsymbol{r}}\cdot\boldsymbol{n}\right],$$

and

$$\frac{\partial}{\partial n}\frac{2D(m)-K(m)}{A^{\frac{1}{2}}} = \frac{1}{A^{\frac{1}{2}}}\left\{\left[\left(\frac{2}{m}-1\right)\frac{\boldsymbol{h}\cdot\boldsymbol{n}}{B} - \left(1-\frac{4}{m}\right)\frac{\hat{\boldsymbol{r}}\cdot\boldsymbol{n}}{2r}\right]E(m) + \left[\left(3-\frac{4}{m}\right)\frac{\hat{\boldsymbol{r}}\cdot\boldsymbol{n}}{2r} - \frac{\boldsymbol{h}\cdot\boldsymbol{n}}{2rR}\right]K(m)\right\},$$

where the vector $\boldsymbol{h}$ is given by

$$\boldsymbol{h} = (Z-z, R-r),$$

where $\hat{\boldsymbol{r}}$ is the unit vector in the r-direction. In these equations $E(m)$ is the complete elliptic function of the second kind. In deriving the above expressions we have used the following relations among the complete elliptic integrals:

$$D(m) = \frac{K(m)-E(m)}{m}, \quad \frac{\mathrm{d}K(m)}{\mathrm{d}m} = \frac{1}{2m}\left(\frac{E(m)}{1-m} - K(m)\right),$$

$$\frac{\mathrm{d}E(m)}{\mathrm{d}m} = \frac{E(m)-K(m)}{2m}, \quad \frac{\mathrm{d}D(m)}{\mathrm{d}m} = \frac{1}{2m^2}\left[\frac{E(m)}{1-m} + E(m) - 2K(m)\right].$$

We make use of the five-term formulae given in Abramowitz & Stegun (1964) for the numerical evaluation of the elliptic functions.

REFERENCES

Abramowitz, M. & Stegun, I. A. 1964 *Handbook of Mathematical Functions*. Washington: Government Printing Office.

Baker, G. R., Meiron, D. I. & Orszag, S. A. 1980 Generalized vortex methods for free-surface flow problems. *J. Fluid Mech.* **123**, 477–501.

Baker, G. R., Meiron, D. I. & Orszag, S. A. 1984 Boundary integral methods for axisymmetric and three-dimensional Rayleigh–Taylor instability problems. *Physica* **12D**, 19–31.

Blake, J. R., Taib, B. B. & Doherty, G. 1986 Transient cavities near boundaries. Part 1. Rigid boundary. *J. Fluid Mech.* **170**, 479–497.

BLAKE, J. R., TAIB, B. B. & DOHERTY, G. 1987 Transient cavities near boundaries. Part 2. Free surface. *J. Fluid Mech.* **181**, 197–212.

CARROLL, K. & MESLER, R. 1981*a* Splashing liquid drops form vortex rings and not jets at low Froude numbers. *J. Appl. Phys.* **52**, 507.

CARROLL, K. & MESLER, R. 1981*b* Part II: Bubble entrainment by drop-formed vortex rings. *AIChE J.* **27**, 853–856.

DOMMERMUTH, D. G. & YUE, D. K. P. 1987 Numerical simulations of nonlinear axisymmetric flows with a free surface. *J. Fluid Mech.* **178**, 195–219.

DOMMERMUTH, D. G., YUE, D. K. P., LIN, W. M., RAPP, R. J., CHAN, E. S. & MELVILLE, W. K. 1988 Deep-water plunging breakers: a comparison between potential theory and experiments. *J. Fluid Mech.* **189**, 423–442.

EDGERTON, H. E. & KILLIAN, J. R. 1954 *Flash.* Boston: Branford.

ENGEL, O. G. 1967 Crater depth in fluid impacts. *J. Appl. Phys.* **37**, 1798–1808.

FRANZ, G. J. 1959 Splashes as sources of sound in liquids. *J. Acoust. Soc. Am.* **31**, 1080–1096.

GUERRI, L., LUCCA, G. & PROSPERETTI, A. 1982 A numerical method for the dynamics of non-spherical cavitation of bubbles. In *Proc. Second Intl Colloquium on Drops and Bubbles* (ed. D. H. Le Croissette), pp. 175–181. Jet Propulsion Laboratory, Pasadena.

HARLOW, F. H. & SHANNON, J. P. 1967*a* The splash of a liquid drop. *J. Appl. Phys.* **38**, 3855–3866.

HARLOW, F. H. & SHANNON, J. P. 1967*b* Distortion of a splashing liquid drop. *Science* **157**, 547–550.

HASHIMOTO, H. & SUDO, S. 1980 Surface disintegration and bubble formation in vertically vibrated liquid column. *AIAA J.* **18**, 442–449.

JASWON, M. A. & SYMM, G. T. 1977 *Integral Equation Methods in Potential Theory and Elastostatics.* Academic.

LIN, W. M. 1984 Nonlinear motion of the free surface near a moving body. Ph.D. thesis, MIT, Dept of Ocean Engineering.

LONGUET-HIGGINS, M. S. & COKELET, E. D. 1976 The deformation of steep surface waves on water. I. Numerical method of computation. *Proc. R. Soc. Lond.* A **350**, 1–26.

LUNDGREN, T. S. & MANSOUR, N. N. 1988 Oscillations of drops in zero gravity with weak viscous effects. *J. Fluid Mech.* **194**, 479–510.

MACKLIN, W. C. & METAXAS, G. J. 1976 Splashing of drops on liquid layers. *J. Appl. Phys.* **47**, 3963–3970.

NYSTUEN, J. A. 1986 Rainfall measurements using underwater ambient noise. *J. Acoust. Soc. Am.* **79**, 972–982.

NYSTUEN, J. A. & FARMER, D. M. 1988 The sound generated by precipitation striking the ocean surface. In *Natural Mechanisms of Surface-Generated Noise in the Ocean* (ed. B. R. Kerman), pp. 485–499. Reidel.

OĞUZ, H. N. & PROSPERETTI, A. 1989 Surface-tension effects in the contact of liquid surfaces. *J. Fluid Mech.* **203**, 149–171.

PROSPERETTI, A., PUMPHREY, H. C. & CRUM, L. A. 1989 The underwater noise of rain. *J. Geophys. Res.* **94**, 3255–3259.

PULLIN, D. I. 1982 Numerical studies of surface-tension effects in nonlinear Kelvin–Helmholtz and Rayleigh–Taylor instability. *J. Fluid Mech.* **119**, 507–532.

PUMPHREY, H. C. & CRUM, L. A. 1988 Acoustic emissions associated with drop impacts. In *Natural Mechanisms of Surface-Generated Noise in the Ocean* (ed. B. R. Kerman), pp. 463–483. Reidel.

PUMPHREY, H. C., CRUM, L. A. & BJØRNØ, L. 1989 Underwater sound produced by individual drop impacts and rainfall. *J. Acoust. Soc. Am.* **85**, 1518–1526.

SCRIMGER, J. A. 1985 Underwater noise caused by precipitation. *Nature* **318**, 647–649.

SCRIMGER, J. A., EVANS, D. J., MCBEAN, G. A., FARMER, D. M. & KERMAN, B. R. 1987 Underwater noise due to rain, hail, and snow. *J. Acoust. Soc. Am.* **81**, 79–86.

SCRIMGER, J. A., EVANS, D. J. & YEE, W. 1989 Underwater noise due to rain – Open ocean measurements. *J. Acoust. Soc. Am.* **85**, 726–731.

WORTHINGTON, A. M. 1894 The splash of a drop and allied phenomena. *Smithsonian Report.* (Reprinted with additions in 1963: *A Study of Splashes.* Macmillan.)